

Anti-Inflammatory Drugs Remodel the Tumor Immune Environment to Enhance Immune Checkpoint Blockade Efficacy



Victoria S. Pelly¹, Agrin Moeini¹, Lisanne M. Roelofsen², Eduardo Bonavita¹, Charlotte R. Bell¹, Colin Hutton³, Adrian Blanco-Gomez³, Antonia Banyard⁴, Christian P. Bromley¹, Eimear Flanagan¹, Shih-Chieh Chiang¹, Claus Jørgensen³, Ton N. Schumacher⁵, Daniela S. Thommen², and Santiago Zelenay^{1,6}

ABSTRACT

Identifying strategies to improve the efficacy of immune checkpoint blockade (ICB) remains a major clinical need. Here, we show that therapeutically targeting the COX2/PGE₂/EP2-4 pathway with widely used nonsteroidal and steroidal anti-inflammatory drugs synergized with ICB in mouse cancer models. We exploited a bilateral surgery model to distinguish responders from nonresponders shortly after treatment and identified acute IFN γ -driven transcriptional remodeling in responder mice, which was also associated with patient benefit to ICB. Monotherapy with COX2 inhibitors or EP2-4 PGE₂ receptor antagonists rapidly induced this response program and, in combination with ICB, increased the intratumoral accumulation of effector T cells. Treatment of patient-derived tumor fragments from multiple cancer types revealed a similar shift in the tumor inflammatory environment to favor T-cell activation. Our findings establish the COX2/PGE₂/EP2-4 axis as an independent immune checkpoint and a readily translatable strategy to rapidly switch the tumor inflammatory profile from cold to hot.

SIGNIFICANCE: Through performing in-depth profiling of mice and human tumors, this study identifies mechanisms by which anti-inflammatory drugs rapidly alter the tumor immune landscape to enhance tumor immunogenicity and responses to immune checkpoint inhibitors.

See related commentary by Melero et al., p. 2372.

INTRODUCTION

Therapeutically targeting immune inhibitory checkpoints through the blockade of PD-1/PD-L1 and CTLA4 has led to unprecedented and durable responses in multiple cancer types (1). Despite this, many patients still fail to respond to immune checkpoint blockade (ICB) owing to poorly understood mechanisms of intrinsic and acquired resistance (2). Moreover, life-threatening immune-related adverse events (irAE) often develop in a significant proportion of patients and remain a major obstacle for the use of ICB, especially in adjuvant and neoadjuvant settings (3). There is therefore an urgent clinical need to better understand, and therapeutically exploit, mechanisms of resistance through the

design of modified treatment regimens including combination therapies (4).

Tumors are infiltrated by a diverse group of immune and nonimmune cells whose functions can have both pro- and antitumorogenic effects. The balance of these opposing inflammatory mediators plays a pivotal role in determining tumor progression and ICB treatment outcome (5, 6). Manipulating the flavor of tumor inflammation thus represents an attractive strategy by which ICB efficacy could be improved, either through combinations with cancer therapies known to have immunostimulatory effects or through direct inhibition of protumorogenic inflammation (4). Cyclooxygenase 2 (COX2) and one of its downstream enzymatic products, prostaglandin E2 (PGE₂), are commonly upregulated in cancer and implicated in multiple aspects of malignant tumor growth such as proliferation, angiogenesis, invasion, and metastasis (7). PGE₂ has also been shown to have pleiotropic effects on immune cell function, and it is increasingly thought that its tumor-promoting functions occur by shaping the tumor immune environment. Accordingly, cancer cell expression of COX2 and production of PGE₂ play a dominant role in tumor immune evasion by directly inhibiting cytotoxic cell function and subsequent adaptive immune responses, in favor of tumor-promoting inflammation (5, 8–10). In addition, COX2 expression anticorrelates with the expression of multiple inflammatory mediators characteristic of so-called “hot” tumors (5) and associated with responses to ICB, such as CXCL9, CXCL10, granzyme B, and IFN γ (11, 12).

The COX2/PGE₂ pathway is therefore a promising target for enhancing the efficacy of ICB and can be therapeutically targeted by a plethora of widely used nonsteroidal anti-inflammatory drugs (NSAID), such as aspirin and selective COX2 inhibitors. Corticosteroids are also thought to exert part of their anti-inflammatory effects through inhibiting COX2 (13). Furthermore, corticosteroids are commonly administered for pain management and treatment-related side effects in cancer patients, including ICB-induced irAEs (3). Past trials have tested NSAIDs, as monotherapy or in combination with

¹Cancer Inflammation and Immunity Group, Cancer Research UK Manchester Institute, The University of Manchester, Alderley Park, Manchester, United Kingdom. ²Division of Molecular Oncology and Immunology, Netherlands Cancer Institute, Amsterdam, the Netherlands. ³Systems Oncology Group, Cancer Research UK Manchester Institute, The University of Manchester, Alderley Park, Manchester, United Kingdom. ⁴Flow Cytometry, Cancer Research UK Manchester Institute, The University of Manchester, Alderley Park, Manchester, United Kingdom. ⁵Division of Molecular Oncology and Immunology, Onco Institute, Netherlands Cancer Institute, Amsterdam, the Netherlands. ⁶The Lydia Becker Institute of Immunology and Inflammation, The University of Manchester, Manchester, United Kingdom.

Note: Supplementary data for this article are available at Cancer Discovery Online (<http://cancerdiscovery.aacrjournals.org/>).

V.S. Pelly and A. Moeini contributed equally as co-first authors of this article.

Corresponding Author: Santiago Zelenay, Cancer Inflammation and Immunity Group, Cancer Research UK Manchester Institute, The University of Manchester, Alderley Park, Macclesfield SK10 4TG, United Kingdom. Phone: 44-161-3066260; E-mail: Santiago.Zelenay@cruk.manchester.ac.uk

Cancer Discov 2021;11:2602–19

doi: 10.1158/2159-8290.CD-20-1815

This open access article is distributed under the Creative Commons Attribution-NonCommercial-NoDerivatives License 4.0 International (CC BY-NC-ND).

©2021 The Authors; Published by the American Association for Cancer Research

cytotoxic therapies, but failed to show a significant improvement in overall survival (7). Instead, more recent retrospective studies have suggested that NSAIDs may enhance the overall survival of patients receiving ICB (14, 15). Rather intriguingly, retrospective analysis has also shown that the overall response rate of patients who discontinued ICB and received corticosteroids is similar to, and in some cases even higher than, that of patients maintained on ICB (16–19).

We have previously shown that genetically targeting the COX2/PGE₂ axis in cancer cells leads to spontaneous immune-dependent tumor control (5, 8, 10) and shifts the tumor micro-environment toward one permissive to ICB responses. Other recent studies also suggest a benefit of therapeutically targeting COX2/PGE₂ to improve the efficacy of immunotherapy including ICB (8, 20–23), although this remains to be tested using clinically applicable regimens. More importantly, the mechanisms underlying the putative synergy between COX2 inhibition and ICB are ill-defined. Here, we set out to test the hypothesis that widely used anti-inflammatory drugs can be repurposed to modulate the intratumoral immune profile and heighten the efficacy of ICB. We show that selectively inhibiting the COX2/PGE₂/EP2-4 axis can lead to rapid remodeling of the environment of both murine and human tumors toward one favorable to ICB efficacy.

RESULTS

Cancer Cell–Intrinsic COX2 Expression Confers Resistance to Immune Checkpoint Blockade

Genetic ablation of cancer cell–intrinsic COX2 results in immune-dependent tumor growth control across a diverse set of murine cancer models (5, 8, 10). In the CT26 colorectal and poorly immunogenic 4T1 breast cancer models, T cells delay the growth of COX-deficient cancer cells, but eventually most mice succumb to progressive tumor growth (8). We took advantage of these two experimental models to test the hypothesis that cancer cell–intrinsic ablation of COX2 sensitizes tumors to ICB and treated mice with 4T1 or CT26 parental (COX2^{WT}) or COX2-deficient (COX2^{KO}) tumors (Supplementary Fig. S1A and B) with anti-PD-1 (α PD-1). Mice with COX2^{WT} 4T1 or CT26 tumors were poorly responsive to PD-1 blockade, whereas several mice bearing COX2^{KO} tumors experienced complete regressions within 2 weeks after treatment and enhanced survival (Fig. 1A; Supplementary Fig. S1C). Restoring COX2 expression in COX2^{KO} 4T1 cells (COX2^{REST}) by retroviral transduction reestablished PGE₂ production (Supplementary Fig. S1A and B) and resistance to α PD-1 therapy (Fig. 1A), demonstrating that tumor-intrinsic COX2 activity may be a powerful resistance mechanism to ICB.

Anti-Inflammatory Drugs Targeting the COX2 Pathway Synergize with ICB to Promote Tumor Control

We next determined whether therapeutic inhibition of COX2 could similarly improve PD-1 blockade efficacy. To test this in a clinically relevant setting, we used celecoxib (CXB), a selective COX2 inhibitor widely prescribed for managing certain inflammatory disorders (<https://www.medicines.org.uk/emc/product/5533/smpc>). To control both the dose and timing of CXB administration, we developed a vehicle for-

mulation that led to its complete solubilization, as opposed to previous studies providing anti-inflammatory drugs *ad libitum* in the drinking water, food, or subcutaneously (8, 22, 23). We treated mice with established CT26 tumors with systemic α PD-1 in combination with a daily oral gavage of CXB (Fig. 1B) at a dose of 30 mg/kg, equivalent to what is considered safe and well tolerated in patients with inflammatory conditions (24). The combination of α PD-1 plus CXB led to greater tumor growth control, with up to 65% of mice exhibiting complete tumor regressions and marked survival benefit compared with either α PD-1 or CXB monotherapy alone (Fig. 1C and D).

More than 50% of patients receiving treatment with combinations of ICB (typically antibodies targeting the PD-1/PD-L1 and CTLA4 pathways) suffer severe irAEs. Most of these patients are withdrawn from ICB treatment and receive systemic corticosteroids to resolve their irAEs (16, 17). One way by which corticosteroids exert their anti-inflammatory effects is through inhibition of the COX2/PGE₂ pathway (13). Indeed, we found that corticosteroids profoundly suppress PGE₂ production by cancer cells to a similar extent as CXB (Supplementary Fig. S1D). Thus, we hypothesized that corticosteroids might also improve the efficacy of ICB. Using the same experimental approach as for CXB, we administered α PD-1 to mice with established CT26 tumors in combination with daily treatment with systemic methylprednisolone for 5 days, followed by daily oral prednisolone, for a total of 3 weeks (MP+P; Fig. 1B), mimicking a regimen commonly used to treat patients suffering from irAEs (25). Notably, the combination of MP+P and PD-1 blockade led to increased tumor eradications and prolonged survival compared with α PD-1 or MP+P monotherapies (Fig. 1E; Supplementary Fig. S1E). To confirm that corticosteroids were exerting their expected pharmacologic activity with this dosing regimen, we monitored the expression of genes directly regulated downstream of the glucocorticoid receptor (26, 27). After 5 days of treatment with methylprednisolone, the levels of *Tat*, *Igfbp1*, and the gene encoding for the glucocorticoid receptor itself, *Nr3c1*, were all altered (Supplementary Fig. S1F). Consistent with its anti-inflammatory properties, methylprednisolone also dampened the expression of *Il1b* and *Il6* in the liver (Supplementary Fig. S1F) and intratumorally (Supplementary Fig. S1G; ref. 13). Given that corticosteroid management of irAEs is more frequently prescribed to cancer patients treated with dual PD-1 and CTLA4 blockade, we next tested the effect of combined therapy with α PD-1/ α CTLA4 and MP+P. In agreement with previous human and mouse studies (28, 29), the dual ICB combination (Supplementary Fig. S1H) was more potent than single treatment with α PD-1 (Fig. 1A). Still, the addition of MP+P led to a trend in further tumor control, enhanced survival, and promoted complete tumor regressions in 85% of animals (Supplementary Fig. S1H).

As methylprednisolone was recently shown to inhibit the efficacy of ICB in a dose-dependent manner (30), we tested PD-1 blockade in combination with a higher dose of corticosteroids. The addition of high-dose MP+P to α PD-1 promoted greater tumor control when assessed 3 weeks after treatment compared with α PD-1 monotherapy, although the combination did not increase the fraction of complete tumor eradications or mouse survival (Supplementary Fig. S1I). Notably, the efficacy

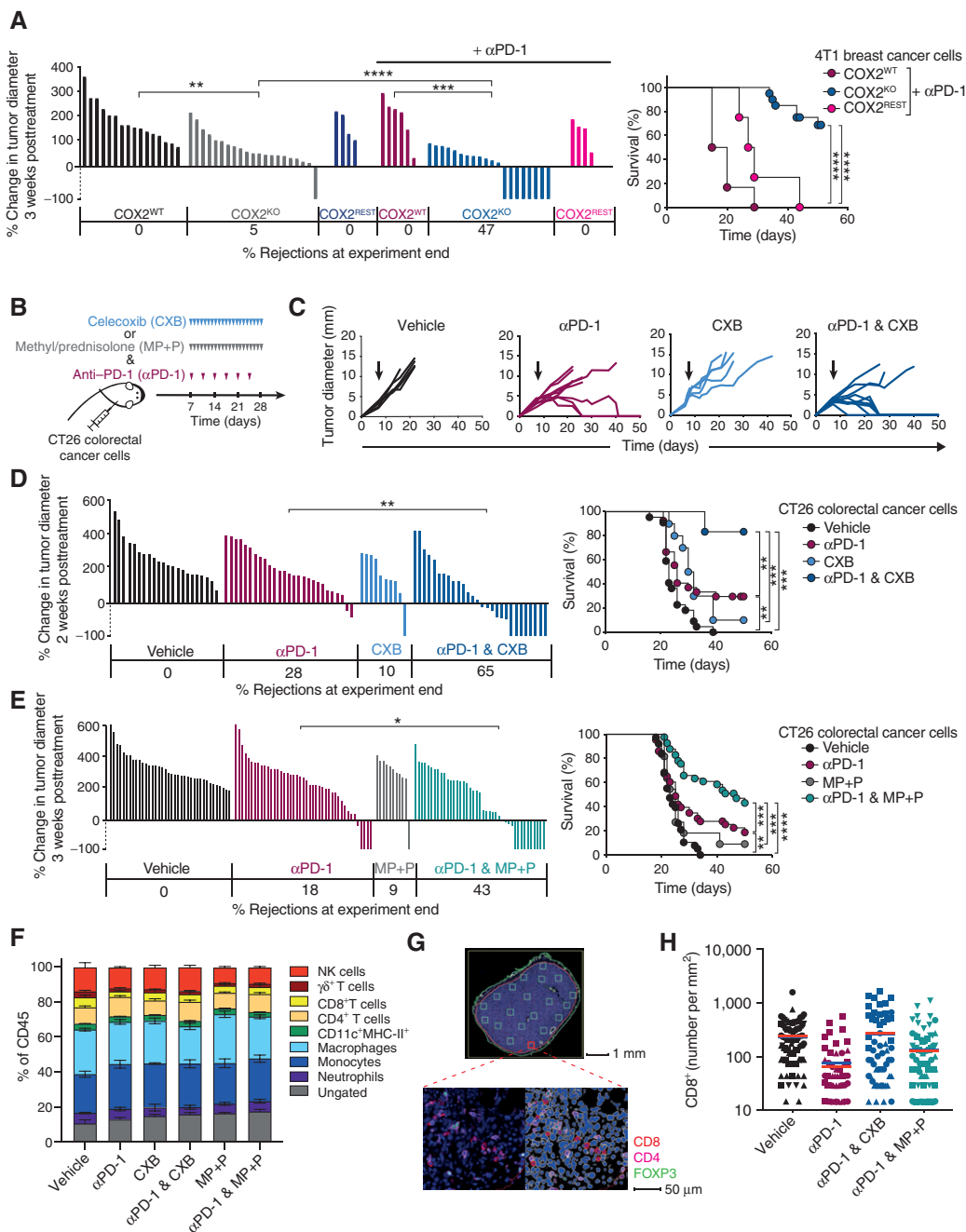


Figure 1. Inhibition of the COX2 pathway via genetic ablation or anti-inflammatory drug treatment synergizes with ICB to overcome immunotherapy resistance. Mice inoculated with parental (COX2^{WT}), COX2-deficient (COX2^{KO}), or COX2-restored (COX2^{REST}) cancer cell lines were treated twice weekly with αPD-1 from day 7 after cancer cell inoculation when tumors were 4.0 ± 1.3 mm in mean diameter. **A**, Left, waterfall plot showing percent change in tumor size 3 weeks after treatment (n = 4–21 per group) and percentage of tumor rejections at experimental endpoint in mice bearing COX2^{WT}, COX2^{KO}, or COX2^{REST} 4T1 breast cancer cells treated with or without αPD-1. Data pooled from 4 independent experiments. Right, Kaplan–Meier survival plots of mice bearing COX2^{WT} (n = 16), COX2^{KO} (n = 20), or COX2^{REST} (n = 4) 4T1 breast cancer cell lines and treated with αPD-1. **B**, Mice inoculated with parental (COX2^{WT}) CT26 colorectal cells were treated with αPD-1 and/or daily anti-inflammatory drugs (CXB or MP+P) from day 7 after cancer cell inoculation when tumor mean diameter was 3.3 ± 1.2 mm. **C**, Individual growth profiles of CT26 colorectal tumors treated with vehicle (n = 5), αPD-1 (n = 9), CXB (n = 5), or αPD-1 + CXB (n = 10). Time of treatment initiation indicated by a black arrow on each growth profile. **D** and **E**, Left, waterfall plot showing percent change in tumor size 2 or 3 weeks after treatment and percentage of tumor rejections at experimental endpoint of mice bearing CT26 colorectal tumors. Right, Kaplan–Meier survival plots of mice bearing CT26 colorectal tumors treated with vehicle, αPD-1, and/or CXB or MP+P (n = 11–43 per group). Data pooled from ≥4 independent experiments. **F**, Frequency of tumor-infiltrating immune cells as a percentage of total leukocytes in CT26 colorectal tumors on day 7 after treatment (n = 5 per treatment group). **G** and **H**, Representative image of multiplex immunofluorescence staining of CD8⁺, CD4⁺, and FOXP3⁺ cells in whole tumor sections (**G**) and quantitation of CD8⁺ T cells in 20 distinct tumor areas pooled from 3–4 mice bearing CT26 colorectal tumors and treated with vehicle, αPD-1 and/or CXB or MP+P for 7 days (**H**). Red line, mean of all tumor areas, blue line, mean of whole tumor area. P value by one-way ANOVA (**A**, **D**, **E**) representing comparisons of major experimental groups and their respective controls only. Log-rank (Mantel–Cox) test of monotherapies versus vehicle or combination versus either of the monotherapies (**A**, **D**, **E**). *, P < 0.05; **, P < 0.01; ***, P < 0.001; ****, P < 0.0001.

Downloaded from <http://aacrjournals.org/cancerdiscovery/article-pdf/11/10/2602/3082297/2602.pdf> by guest on 07 November 2024

of α PD-1 and high-dose MP+P was fully lost in immune-deficient NSG mice, excluding the possibility that tumor control was independent of the immune system (Supplementary Fig. S1I). Concomitant administration of a different corticosteroid, dexamethasone, similarly improved α PD-1 treatment (Supplementary Fig. S1I). Finally, mice that had eradicated tumors after α PD-1 treatment with either CXB or MP+P spontaneously rejected tumor rechallenges without further treatment, indicating that the development of long-term immunity was not compromised by the use of CXB or MP+P (Supplementary Fig. S2A). In conclusion, these data demonstrated that NSAIDs, as well as corticosteroids widely used for their immunosuppressive effects, can paradoxically enhance the efficacy of ICB in preclinical cancer models.

Anti-Inflammatory Drugs in Combination with ICB Alter the Molecular but Not the Cellular Tumor Inflammatory Landscape

Together, these results suggested that anti-inflammatory drugs can actually foster the type of inflammation that favors immune-mediated cancer control. To test this hypothesis, we characterized the tumor immune cell infiltrate by multiparameter flow cytometry. To identify the causal basis for the enhanced tumor control observed after combination therapy, and to avoid potential confounding effects of analyzing tumors of different sizes, we examined size-matched tumors collected 1 week after treatment with α PD-1 with or without the addition of CXB or MP+P (Supplementary Fig. S2B). We found no overt changes in the overall tumor infiltrate composition in either myeloid or lymphoid compartments across the different treatment arms (Fig. 1F). Analysis of tumor sections by immunofluorescence also failed to reveal clear differences in the abundance and spatial distribution of CD8⁺, CD4⁺ T cells or FOXP3⁺ regulatory T cells (Fig. 1G and H; Supplementary Fig. S2C). In spite of the lack of alterations in overall leukocyte composition, the transcript levels of mediators associated with COX2-driven cancer-promoting inflammation such as IL6 and IL1 β (5, 8) were reduced in tumors from animals receiving the combination of α PD-1 with CXB or MP+P, although the difference for IL6 did not reach statistical significance in the latter group (Supplementary Fig. S2D).

Transcriptomic Profiling Using a Bilateral Tumor System Uncovers an Early IFN-Driven Inflammatory Program Associated with ICB Responses

We hypothesized that a possible explanation for the lack of noticeable changes in leukocyte composition in mice receiving α PD-1 plus CXB could be the inherent dichotomy in responses across treatment groups. Indeed, despite the remarkable synergy between ICB and anti-inflammatory drugs, we consistently found that a fraction of animals remained unresponsive to treatment across all our experimental systems, similar to what is seen in patients (28). We reasoned that the identification of primary mechanisms underpinning treatment synergy would be greatly confounded by this heterogeneity in responses. To overcome this limitation, we developed a bilateral tumor surgery model that would allow us to distinguish responders from nonresponders early after treatment. In this model, 1 of the 2 tumors in mice receiving α PD-1 or α PD-1 plus CXB was surgically removed 1 week after treatment for

RNA-sequencing (RNA-seq) analysis, while the contralateral tumor continued to be monitored to determine treatment outcome (Fig. 2A). In agreement with recent studies exploiting a similar experimental setup (31, 32), we established that responses to α PD-1 or α PD-1 plus CXB were concordant between contralateral tumors. Indeed, in 90% of mice, both tumors in a single mouse either grew progressively or were completely rejected, irrespective of treatment (Supplementary Fig. S3A; Supplementary Table S1). We were therefore able to infer with high confidence the response outcome of the surgically resected tumors based on the progressive [non-responder (NR)] or regressive [responder (R)] growth of the contralateral tumor. Consistent with our previous data, the addition of CXB improved the efficacy of α PD-1 in a large proportion of mice; however, a substantial fraction remained unresponsive to either regimen (Fig. 2B).

Unsupervised *k*-means clustering on the transcriptome of all surgically resected tumors from mice treated with either α PD-1 or α PD-1 plus CXB revealed 2 major transcriptional programs that were significantly enriched in samples originating from either R or NR mice ($P = 0.038$, 2-tailed Fisher exact test, Fig. 2C; Supplementary Fig. S3B). Among the top differentially upregulated genes in the R cluster, many were characteristic of cytotoxic T-cell activity, including *Cd8a*, *Cd8b1*, *Gzmd*, and *Ifng* (Fig. 2C; Supplementary Fig. S3C). To further characterize the biological processes underlying the transcriptional changes defining R and NR clusters, we performed gene set enrichment analysis (GSEA) using the MSigDB hallmark gene set collection. This analysis showed profound enrichment of “IFN γ response” as well as many other immune-related and inflammatory pathways in the R cluster (Fig. 2D; Supplementary Table S2). Conversely, the NR cluster was enriched in gene sets associated with protumorigenic processes such as “epithelial mesenchymal transition,” “G2M checkpoint,” and “Myc targets,” whose expression was recently associated with lack of responses in patients with melanoma receiving single or combination ICB (12). Likewise, Ingenuity Pathway Analysis (IPA) revealed enrichment of many genes within the IFN γ pathway, and both IFNG and STAT1 were predicted as the main upstream regulators of the R cluster (Supplementary Fig. S3D and E; Supplementary Table S3).

Next, we inferred the cellular infiltrate composition of tumors from R and NR clusters using the microenvironment cell populations (MCP) counter (33) and Consensus (34) methods. In agreement with the tumor fate, this analysis revealed a highly significant enrichment in CD8, cytotoxic, T, and natural killer (NK) cell populations as well as in the total Immunoscore, which represents the total level of immune infiltration in each tumor sample (34) within the R cluster (Fig. 2E; Supplementary Fig. S3F). Conversely, the NR cluster was enriched in signatures of endothelial cells, fibroblasts, and angiogenesis. Thus, an unbiased approach to examine the transcriptome of on-treatment responders early after treatment uncovered the induction of an intratumoral molecular program characterized by the upregulation of multiple IFN-driven genes and infiltration by immune populations typically associated with responses to ICB in patients.

We wondered whether this acute IFN response program that preceded tumor eradication, referred to hereafter as acute IFN response (AIR), would similarly associate with

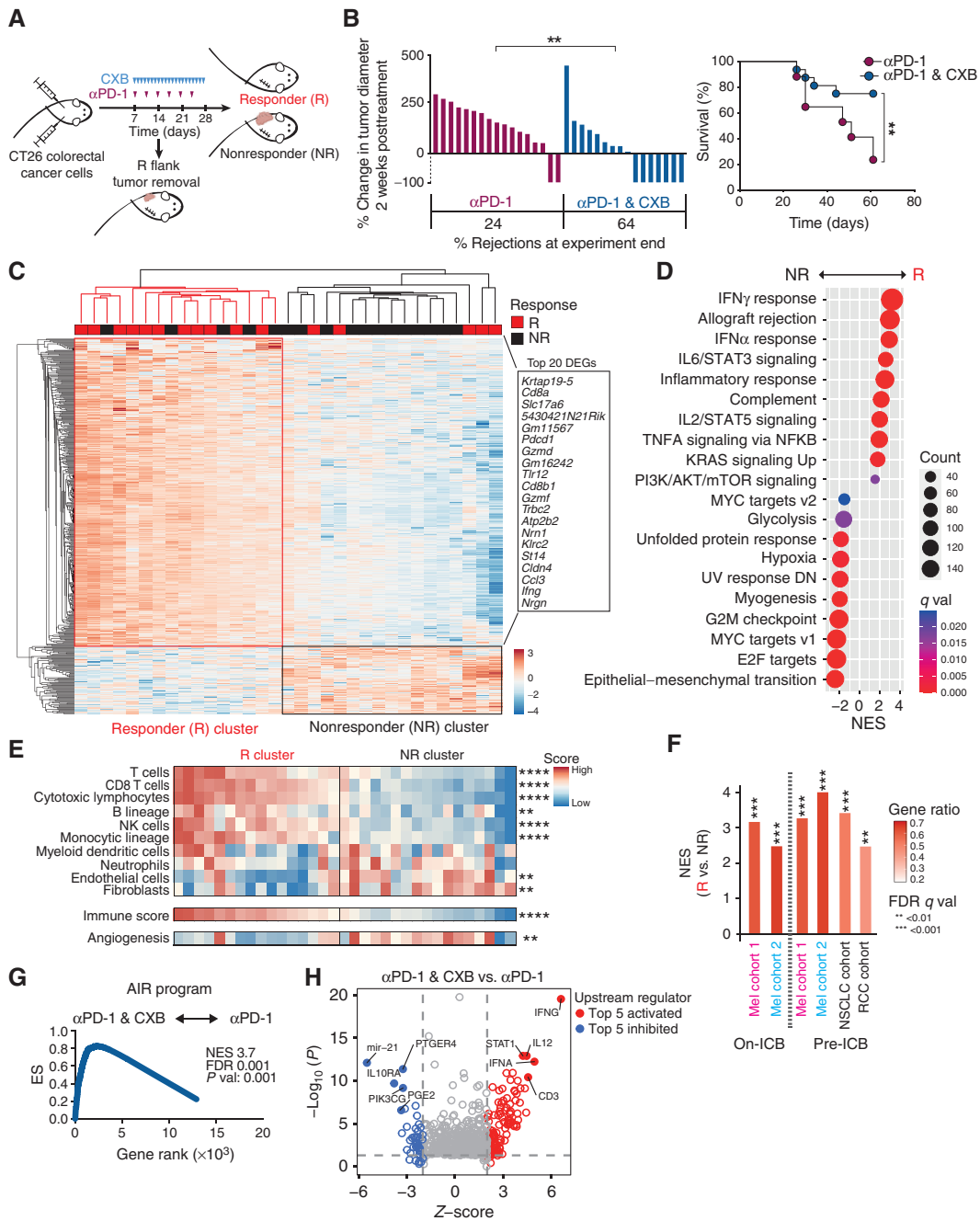


Figure 2. Bilateral surgery model uncovers a distinct immune molecular landscape associated with response to ICB. **A**, Mice were inoculated bilaterally with CT26 colorectal cells and treated with α PD-1 alone or in combination with CXB from day 7 after cancer cell inoculation when tumors were 4.0 ± 1.0 mm in mean diameter. Right flank tumors were surgically excised on day 7 after treatment, and left flank tumor growth was monitored until experiment end to determine response outcome. **B**, Left, waterfall plot showing percent change in tumor size 2 weeks after treatment and percentage of tumor rejection at experimental endpoint in remaining contralateral tumors ($n = 16$ – 17 per group). P value by Mann-Whitney U test. Right, Kaplan-Meier survival plots of the bilaterally CT26 implanted mice treated with α PD-1 alone ($n = 17$) or combined with CXB ($n = 16$). P value by log-rank (Mantel-Cox) test. **C**, Hierarchical clustering and heat-map representation of top differentially expressed genes between responder (red) and nonresponder (black) clusters obtained by non-negative matrix factorization k -means consensus clustering. **D**, Dot plot representation of top 10 significantly differentially enriched pathways in samples belonging to the responder and nonresponder clusters identified by GSEA of Hallmark gene sets. count, number of genes contributing to the enrichment score; q value, false discovery rate; NR, nonresponder; R, responder. **E**, Heat-map representation of the abundance (score) of 10 cell populations, angiogenesis, and immune score in samples from R and NR clusters, calculated using the MCP-counter and Consensus methods. P value by Mann-Whitney U test. **F**, Bar plot representation of significant enrichment of the AIR program in R (complete and partial responders) in comparison with NR (stable disease and progressive disease) patients either on or pretreatment with ICB. Gene ratio denotes the percentage of genes within the AIR program contributing to the enrichment score. Mel, melanoma. **G**, Enrichment plot of the AIR program genes showing significant enrichment in α PD-1 and CXB versus α PD-1 treatment in CT26 tumors on day 7 after treatment. **H**, Volcano plot of predicted upstream regulators by IPA based on the differentially expressed genes between α PD-1 and α PD-1 & CXB treatment in CT26 tumors on day 7 after treatment. Significantly activated and inhibited upstream molecules are highlighted in red and blue, respectively. ES, enrichment score; FDR, false discovery rate; NES, normalized enrichment scores. **, $P < 0.01$; ***, $P < 0.001$; ****, $P < 0.0001$.

responses in patients treated with ICB. To test this, we interrogated two separate cohorts of α PD-1-treated patients with melanoma with available transcriptional profiles from on-treatment tumor biopsies (Supplementary Table S4). In agreement with the murine findings, the AIR program was enriched in on-treatment samples from responders compared with nonresponders (Fig. 2F). This association also extended to pretreatment samples in melanoma and other cancer types including non-small cell lung (NSCLC) and renal cell cancer (RCC; Fig. 2F; Supplementary Table S4), in line with IFN γ signaling being a feature of “hot” tumors and a major contributor to ICB efficacy (11, 12). In conclusion, a bilateral surgery model was able to capture the heterogeneity in treatment outcomes and identified the early activation of an intratumoral molecular program linked to immunotherapy responses in both mouse and patient tumors.

PGE₂ Receptor Antagonists Phenocopy COX2 Inhibition and Synergize with ICB Treatment

Having identified a transcriptional response preceding ICB-driven tumor control, we next tested whether the addition of CXB to ICB would induce the AIR program irrespective of treatment outcome. The AIR program was indeed significantly enriched in tumors from mice treated with α PD-1 plus CXB compared with α PD-1 alone (Fig. 2G), in accordance with their increased responses to treatment. Furthermore, IPA on differentially expressed genes (DEG) between tumors from α PD-1 and CXB versus α PD-1-treated mice also identified IFN γ as the top upstream regulator (Fig. 2H; Supplementary Table S3). Conversely, PGE₂ and its receptor EP4 (encoded by PTGER4) were among the most inhibited upstream regulators. These data suggested that the heightened IFN γ response after addition of CXB to PD-1 blockade might have occurred as a result of dampening PGE₂ synthesis and downstream signaling through its specific receptors. This hypothesis is in line with our recent finding that PGE₂ promotes cancer immune escape by signaling through its specific receptors EP2 and EP4 on the surface of cytotoxic cells (5).

As well as PGE₂ synthesis, COX2 is required for the synthesis of multiple inflammatory mediators including leukotrienes, thromboxanes, and other prostaglandins with known pro- or antitumorogenic functions (7). Thus, therapeutically targeting EP2 and EP4 could represent a more selective approach to limit the immunosuppressive functions of PGE₂ while simultaneously sparing cancer-restraining prostaglandins and avoiding potential adverse effects associated with COX2 inhibition (35). We therefore tested whether selective EP2 and EP4 antagonists would mimic COX2 inhibition and enhance the efficacy of PD-1 blockade. In a regimen analogous to the one used for dosing CXB by oral gavage, we treated mice with established CT26 colorectal or 5555 *Braf*^{N600E}-driven melanoma tumors, on a BALB/c or C57BL/6 background, respectively, with α PD-1 in combination with twice-daily doses of a mix of both EP2 and EP4 antagonists (EPAT; Fig. 3A). Compared with monotherapy treatment with either α PD-1 or EPAT, which did not induce tumor control, their combination led to a significant number of tumor eradications and increased overall survival in both cancer models (Fig. 3B; Supplementary Fig. S4A). Mice that had rejected tumors after either α PD-1 or α PD-1 plus EPAT were resistant

to further rechallenge with parental cells (Supplementary Fig. S4B), indicating the development of long-term immunity, similar to regimens combining immunotherapy with CXB or MP+P. These data suggested that selective COX2 inhibitors potentiate ICB therapy primarily by inhibiting PGE₂ synthesis and EP2-4 downstream signaling.

To test whether the combination of PD-1 blockade and EP2-4 antagonism promoted a shift in the transcriptional landscape of tumors similar to that induced by α PD-1 plus CXB, we treated mice with α PD-1 and/or EPAT and harvested tumors for transcriptional profiling by RNA-seq. To investigate the temporal kinetics of the changes induced by the single treatments or their combination, we analyzed 5555 melanoma tumors at 2 and 5 days on-treatment. As early as 2 days, the AIR program was significantly enriched in α PD-1-treated mice compared with vehicle (Supplementary Fig. S4C), in line with a reported peak in IFN γ production 2 days after α PD-1 treatment (36). Notably, single treatment with EPAT led to the induction of the AIR program at day 2 as well as day 5, an effect that was also observed in CT26 colorectal tumors after CXB monotherapy (Fig. 3C; Supplementary Fig. S4D). These data suggested that inhibition of PGE₂ synthesis or downstream signaling via EP2-4 has rapid effects on the intratumoral transcriptional landscape comparable to those of PD-1 blockade. To further examine this possibility, we performed unsupervised hierarchical clustering on genes differentially expressed between tumors from mice treated with α PD-1, EPAT, or their combination compared with vehicle-treated control mice on day 2 after treatment. Tumors treated with either α PD-1 or EPAT clustered separately from the majority of vehicle-treated tumors and largely intermingled (Fig. 3D), suggesting they had comparable changes in their transcriptional profile. Interestingly, these changes were more pronounced in mice that received the combination of α PD-1 plus EPAT, which clustered farthest from vehicle-treated tumors (Fig. 3D), as demonstrated by their greater Euclidean distance from vehicle (Fig. 3E). These findings were further supported by IPA and GSEA. Indeed, the most highly enriched upstream regulators and hallmark gene sets, including IFNG and STAT1, were common between all three regimens (Fig. 3F and G; Supplementary Table S3); however, the combination of α PD-1 plus EPAT induced the most significant shift (Fig. 3G). Collectively, these data indicated that simultaneous blockade of PD-1 and PGE₂ receptor signaling can acutely remodel the tumor landscape toward a transcriptional profile associated with ICB benefit in mice and humans. Crucially, single targeting of PGE₂ production or signaling induced similar changes, albeit to a lower degree, suggesting that inhibition of the COX2/PGE₂/EP2-4 axis might present a readily available strategy to rapidly render tumors more permissive to anticancer effector T cells.

COX2/PGE₂/EP2-4 Inhibition Leads to Abrupt but Transient IFN γ -Driven Inflammatory Signaling in the Tumor Microenvironment

To further explore the potential of COX2/PGE₂/EP2-4 targeting as a means to turn the molecular profile of tumors from cold to hot, we treated tumor-bearing mice with either CXB or EPAT monotherapy twice daily for 2 days and determined the expression levels of immune mediators classically

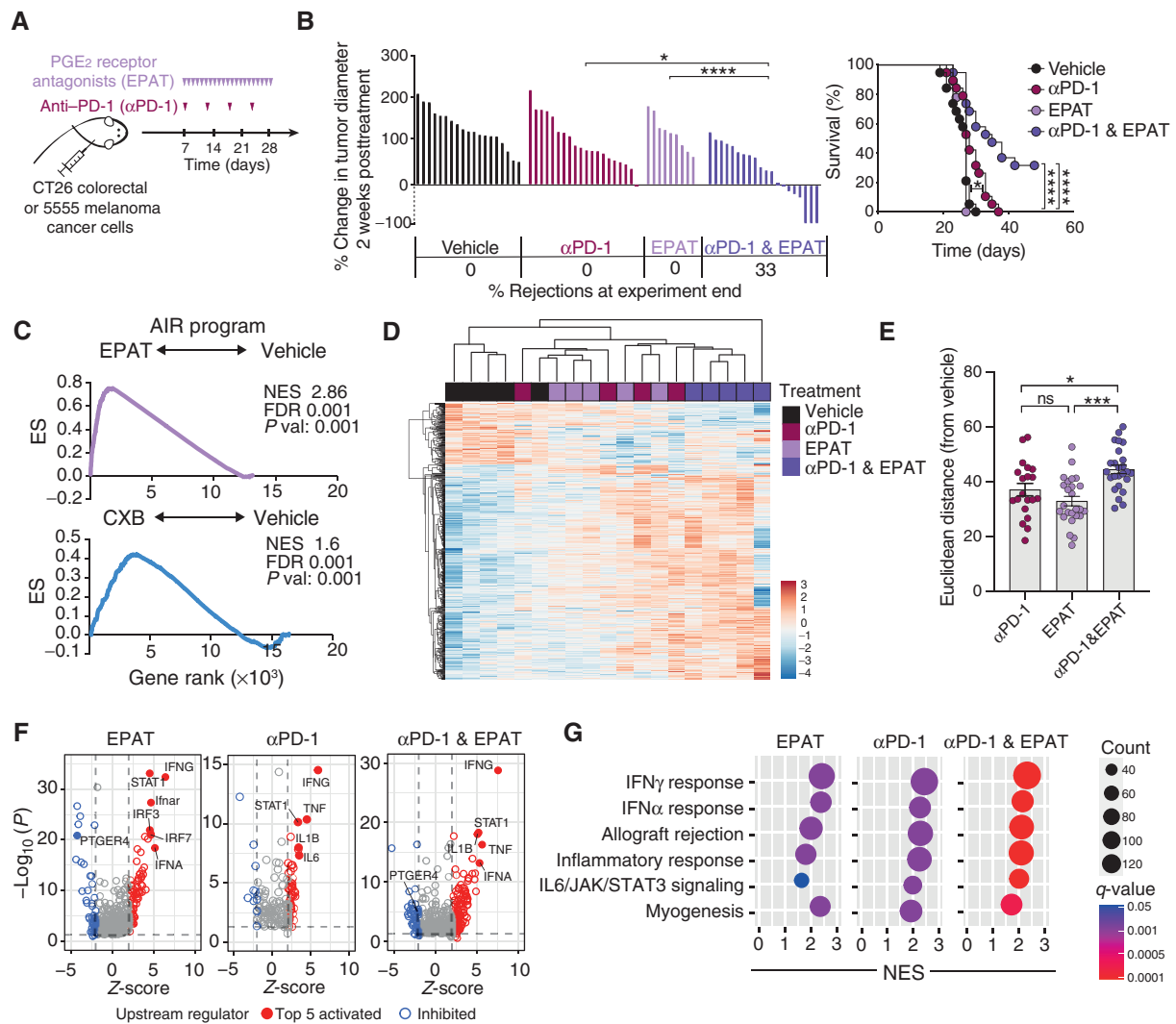


Figure 3. Inhibition of PGE₂ synthesis or downstream receptor signaling synergizes with ICB to promote the molecular program associated with response to immunotherapies. **A**, Experimental model representing the inoculation of cancer cell lines in wild-type mice treated with 4 doses of αPD-1 and/or twice-daily doses of a mix of EP2 and EP4 receptor antagonists (EPAT) from day 7 after cancer cell inoculation when tumors were 4.8 ± 0.7 mm in mean diameter. **B**, Left, waterfall plot showing percent change in tumor size 2 weeks after treatment and percentage of tumor rejection at experimental endpoint of 5555 melanoma-bearing mice treated with vehicle, αPD-1, and/or EPAT ($n = 10$ – 20 per group). Data represent 3 independent experiments. P value by one-way ANOVA representing comparisons of major experimental groups and their respective controls only. Right, Kaplan-Meier survival plots of experimental groups. P value by log-rank (Mantel-Cox) test of monotherapies versus vehicle or combination versus either of the monotherapies. **C**, Enrichment plot of the AIR program genes showing significant enrichment in EPAT or CXB versus vehicle-treated 5555 melanoma tumors on day 2 or 7 after treatment, respectively. **D**, Hierarchical clustering and heat-map representation of differentially expressed genes upon treatment with αPD-1 and/or EPAT in comparison with vehicle controls in 5555 melanoma tumors on day 2 after treatment. **E**, Mean delta Euclidean distance between αPD-1 and/or EPAT compared with vehicle, paired analysis of each treated sample versus vehicle controls. P value by one-way ANOVA followed by multiple comparisons test. **F**, Volcano plot of predicted upstream regulators by IPA based on the differentially expressed genes between each treatment group and vehicle controls in melanoma tumors on day 2 after treatment. Significantly activated and inhibited upstream molecules are highlighted in red and blue, respectively. **G**, Dot plot representation of top significantly differentially enriched pathways in each treatment group in comparison to vehicle treatment in melanoma tumors on day 2 after treatment as identified by GSEA of hallmark gene sets. Count, number of genes within each gene set contributing to the enrichment score q value, false discovery rate. *, $P < 0.05$; ***, $P < 0.001$; ****, $P < 0.0001$.

associated with cancer-inhibitory (CI) T-cell inflammation (5) by quantitative PCR (qPCR; Supplementary Fig. S5A). Unsupervised clustering revealed 2 major clusters, 1 of which was significantly enriched in tumors treated with either CXB or EPAT ($P < 0.0001$, 2-tailed Fisher exact test, Fig. 4A). We found a marked increase in the expression of multiple CI genes (Supplementary Table S1) including *Ifng*, *Cxcl10*, *Gzmb*, *Prfl*, *Tbet*, *Cd274* (PD-L1), and *Il12b* in CXB- and EPAT-treated

melanoma or colorectal tumors compared with control mice (Fig. 4A and B; Supplementary Fig. S5B). Conversely, CXB and EPAT treatments reduced the expression of COX2-driven cancer-promoting (CP) genes such as *Vegfa*, *Il6*, and *Ptgs2* (Fig. 4A; Supplementary Table S1). As a result, the COX2-associated inflammatory signature (COX-IS), which integrates pro- and antitumorigenic inflammatory factors and negatively associates with ICB benefit in multiple cancer types (5), was

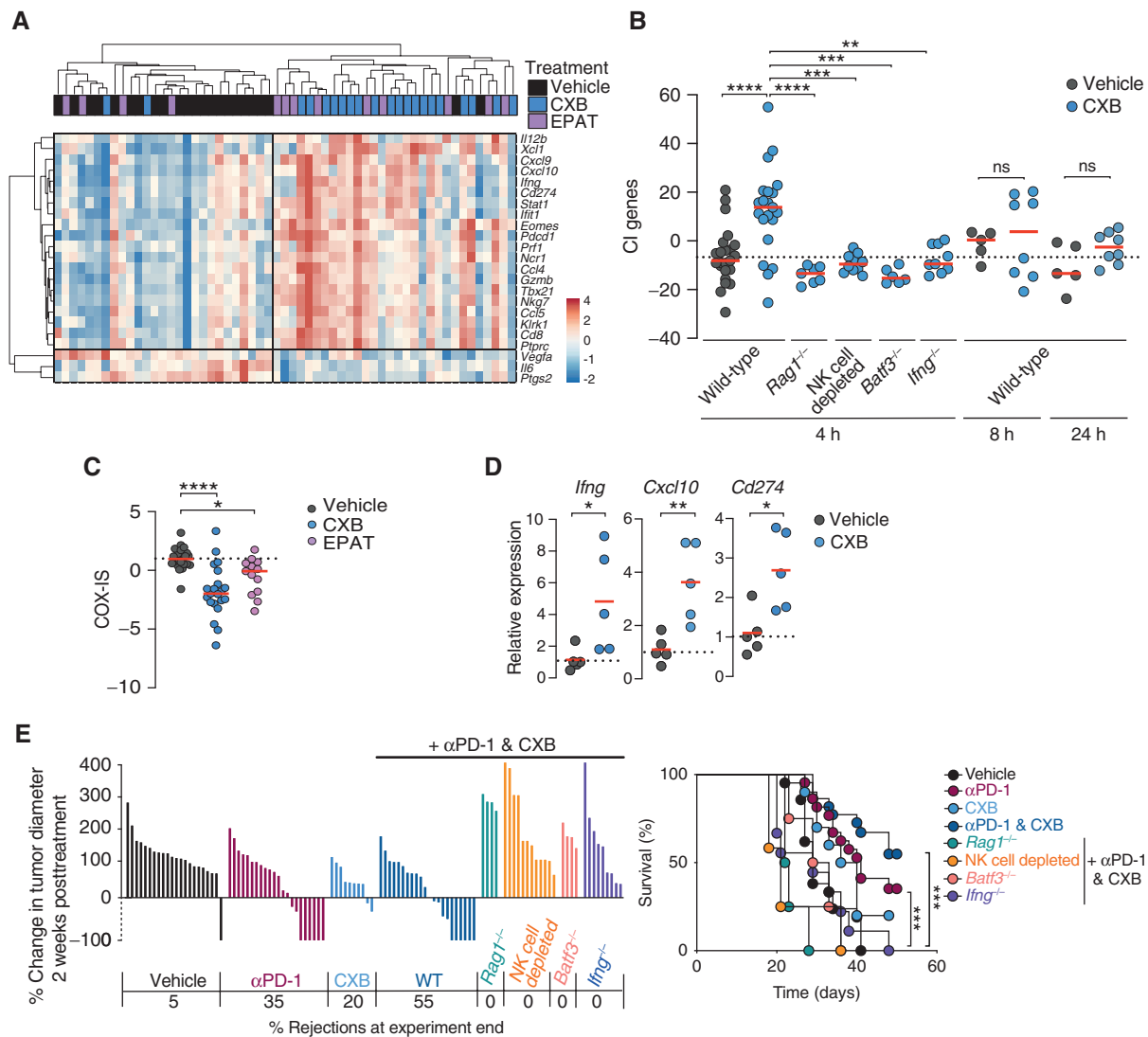


Figure 4. COX-2/PGE₂ pathway inhibition acutely and transiently activates IFN γ signaling in the tumor microenvironment. **A**, Hierarchical clustering and heat-map representation of significantly deregulated immune mediators classically associated with cancer-inhibitory or cancer-promoting inflammation, top and bottom cluster of genes, respectively, measured by qPCR in melanoma tumors on day 2 after treatment with CXB or EPAT monotherapy in comparison with vehicle. Pooled data from ≥ 3 independent experiments. **B**, Time course of induction of cancer-inhibitory (CI) gene expression after the final dose of CXB represented as the fold change of cumulative z-scores relative to vehicle controls in wild-type, immunodeficient, or NK-depleted mice bearing melanoma tumors ($n = 6$ –20 mice per group from ≥ 2 independent experiments). **C**, COX-IS measured by qPCR in melanoma tumors on day 2 after treatment with CXB or EPAT monotherapy in comparison with vehicle ($n = 10$ –20 mice per group from 3 independent experiments). **D**, Induction of *Ifng* or IFN γ -stimulated genes 4 hours after a single dose of CXB in melanoma tumors detected by qPCR and expressed relative to *Hprt* expression. **E**, Left, waterfall plot showing percent change in tumor diameter 2 weeks after treatment and percentage of tumor rejections at experimental endpoint. Right, Kaplan-Meier survival plots of 5555 melanoma tumor-bearing WT mice treated with vehicle, α PD-1, and/or CXB or immunodeficient or NK-depleted mice treated with α PD-1 plus CXB ($n = 4$ –22 per group from 1–3 independent experiments). *P* value by log-rank (Mantel-Cox) test, showing significance of α PD-1 or α PD-1 plus CXB versus vehicle in wild-type mice (****, $P < 0.0001$), or α PD-1 plus CXB in wild-type mice versus α PD-1 plus CXB evaluated in either *Rag1*^{-/-}, *Batf3*^{-/-}, *Ifng*^{-/-} or NK cell-depleted mice (****, $P < 0.001$). *P* value by one-way ANOVA (**B** and **C**) and unpaired t test (**D**). *, $P < 0.05$; **, $P < 0.01$; ***, $P < 0.001$; ****, $P < 0.0001$.

significantly reduced by CXB or EPAT treatment (Fig. 4C; Supplementary Fig. S5C). Strikingly, CI mediators including hallmark IFN γ -stimulated genes encoding CXCL10, PD-L1, and IFN γ itself were significantly upregulated 4 hours after a single dose of CXB (Fig. 4D; Supplementary Fig. S5D). This rapid increase in CI genes was highest 4 hours after treatment and progressively lost over a 24-hour period without CXB redosing (Fig. 4B). This is consistent with the pharmacokinetics of CXB (<https://www.medicines.org.uk/emc/>

product/5533/smpc) and implies that sustained COX2 inhibition might be required for maximum synergy with ICB.

To investigate the cellular and molecular mediators responsible for the expression of CI mediators after CXB treatment, we treated 5555 melanoma-bearing *Rag1*^{-/-} or *Batf3*^{-/-} mice, lacking mature T and B cells or type I conventional dendritic cells (cDC1), respectively, with CXB for 2 days and analyzed their tumors 4 hours after the last dose. The levels of CI genes in both CXB-treated *Rag1*^{-/-} or *Batf3*^{-/-} mice were significantly

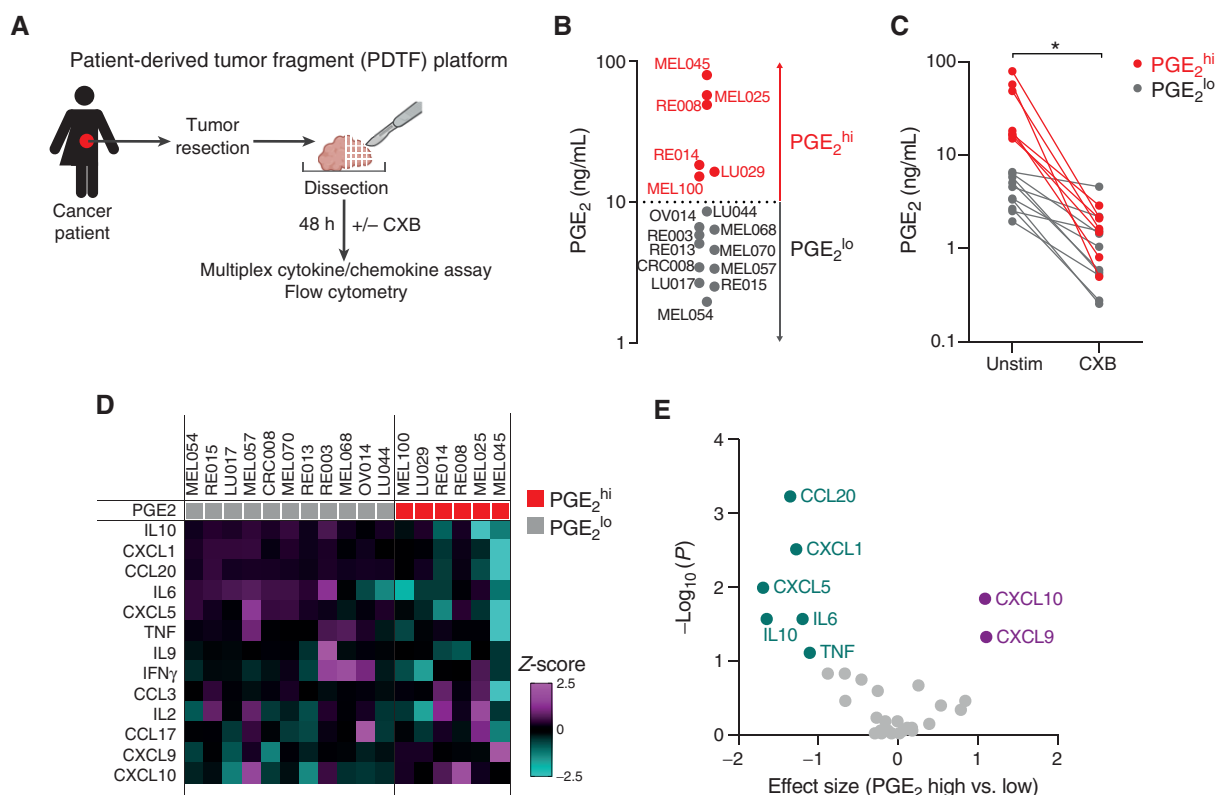


Figure 5. COX2 inhibition alters the inflammatory milieu of PDTF by suppressing multiple inflammatory markers and enhancing CXCL9 and CXCL10 production. **A**, PDTF platform: surgically resected patient tumors are dissected into fragments and cultured in medium with or without CXB for 48 hours before analysis. **B**, PGE₂ concentration in the supernatant of PDTFs from 17 independent tumors after 48 hours of culture in medium. **C**, PGE₂ concentration in the supernatant of PDTFs after 48 hours of culture in medium alone or with CXB. *P* value by paired *t* test. Unstim, unstimulated. **D**, Heat map showing the change in cytokine and chemokine concentration induced by CXB relative to medium alone. **E**, Volcano plot showing the effect size for each factor comparing PGE₂^{hi} versus PGE₂^{lo} tumors. Effect size (calculated using Hedge *g*) and *P* values (2-tailed Mann-Whitney test) of significantly increased and decreased proteins (*P* < 0.05) are highlighted in purple and green, respectively. *, *P* < 0.05.

lower compared with CXB-treated wild-type animals (Fig. 4B; Supplementary Fig. S5E). Likewise, the expression of CI genes was markedly reduced in mice acutely depleted of NK cells, in line with a role for NK cells in orchestrating the adaptive immune response in COX2-deficient tumors or when rendered insensitive to PGE₂ (5). The rapid induction of CI genes was also lost in IFN γ -deficient (*Ifng*^{-/-}) mice treated with CXB (Fig. 4B), consistent with the finding that IFN γ was predicted to be upstream of the transcriptional changes after COX2 inhibition. Finally, tumor-bearing *Rag1*^{-/-}, NK cell-depleted, *Batf3*^{-/-}, or *Ifng*^{-/-} mice did not benefit from α PD-1 and CXB treatment (Fig. 4E), uncovering a central role of the NK/cDC1/T-cell axis and IFN γ for the therapeutic benefit of combining inhibitors of the COX2/PGE₂ pathway with ICB.

COX2 Inhibition Dampens Cancer-Promoting Mediators and Stimulates Cancer-Inhibitory Inflammation in Human Tumors

Next, we used a novel patient-derived tumor fragment (PDTF) platform (37) to test whether monotherapy with CXB could similarly shape the human inflammatory tumor microenvironment. Tumor specimens obtained from surgical resections from treatment-naïve patients were dissected into tissue fragments and cultured *ex vivo* in the presence or

absence of CXB. The changes in cellular and secretory profiles of these PDTFs were analyzed 48 hours later by flow cytometry and multiparameter cytokine and chemokine arrays (Fig. 5A). We tested 17 independent tumors of multiple tissue origins: melanoma (*n* = 7) and lung (*n* = 3), colorectal (*n* = 1), ovarian (*n* = 1), and kidney (*n* = 5) cancer (Supplementary Table S5). Six of these produced high levels of PGE₂ (>10 ng/mL; referred to as PGE₂^{hi}) upon 48 hours of culture (Fig. 5B). The cellular immune and nonimmune baseline composition of these tumors was heterogeneous; however, PGE₂ levels did not obviously associate with cancer type or cell composition (Supplementary Fig. S5F). As expected, addition of CXB to the culture medium significantly inhibited PGE₂ release (Fig. 5C). This was associated with a distinct shift in the cytokine and chemokine profile of PGE₂^{hi} compared with PGE₂^{lo} PDTFs, in accordance with their more pronounced reduction in PGE₂ levels after treatment (Fig. 5D and E). In line with our murine data, COX2 inhibition led to a significant increase in the levels of CXCL9 and CXCL10 and concomitant dampening of immunosuppressive factors such as IL6, IL10, CXCL1, and CXCL5 (Fig. 5E). Thus, CXB treatment of multiple independent PGE₂-producing human tumors resulted in a rapid switch in the tumor immune environment toward one conducive to T-cell accumulation and effector activity.

Concomitant COX2 Inhibition during PD-1 Blockade Enhances T-cell Effector Function

Having identified rapid and distinct changes in hallmark cytokines and chemokines associated with T-cell infiltration and effector function after treatment with α PD-1, CXB, or their combination, we next examined the extent to which the activation phenotype of tumor-infiltrating T cells was changed as a consequence. For this, we analyzed on-treatment immune cell infiltrates by multicolor flow cytometry and cytometry by time-of-flight (CyTOF) at the onset of 5555 melanoma shrinkage after ICB treatment, when tumors were still comparable in size. The overall composition of most lymphoid and myeloid cell subsets was only moderately changed across treatment groups (Fig. 6A), in line with our earlier data in the CT26 colorectal model (Fig. 1F). There was, however, a decrease in macrophage and an increase in CD8⁺ T-cell relative abundance, but not absolute number, in the α PD-1 plus CXB-treated mice compared with vehicle and α PD-1 monotherapy treatment (Fig. 6A; Supplementary Fig. S5G). Hierarchical clustering of >20 surface and intracellular proteins (Supplementary Table S6) used to discriminate CD8⁺ T-cell functional states (38) revealed two distinct expression patterns across treatment groups (Fig. 6B). Notably, the expression levels of a cluster of markers associated with T-cell dysfunction such as TOX, TIM3, and LAG3 (38) tended to be lower in mice receiving α PD-1 plus CXB compared with α PD-1- or vehicle-treated mice (Fig. 6B; Supplementary Table S7). Conversely, the expression of proteins associated with activation and cytotoxic T-cell function such as Granzyme B, TBET, and TCF1, a transcription factor associated with a naïve-like CD8⁺ T-cell phenotype required for PD-1 blockade efficacy (38), were higher in CD8⁺ T cells infiltrating α PD-1 plus CXB-treated tumors (Fig. 6B). Unsupervised clustering of CD8⁺ T cells into 7 cell states (Fig. 6C; Supplementary Fig. S5H and I; Supplementary Table S7) further highlighted the phenotypic switch of CD8⁺ T cells in mice receiving α PD-1 plus CXB. Indeed, a cluster of cells expressing high levels of exhaustion markers (Cluster 6, Fig. 6D; Supplementary Fig. S5I) including CD39 and TOX, was proportionately reduced in mice treated with α PD-1 plus CXB (Fig. 6D). Conversely, tumors from this treatment group showed enrichment in a CD8⁺ T-cell cluster expressing Granzyme B, low levels of EOMES, and intermediate levels of exhaustion markers (Cluster 3, Supplementary Fig. S5I and J) and an increase in the infiltration of naïve-like CD8⁺ T cells with high TCF1 and CD62L expression and lower PD-1 levels (Cluster 1, Fig. 6E; Supplementary Fig. S5I). This

was associated with an expansion of activated CD4⁺ T cells expressing higher levels of CD25, PD-1, and TBET (Fig. 6F) and enhanced IFN γ production by both CD8⁺ and CD4⁺ T cells (Fig. 6G). Collectively, this analysis indicated that concomitant COX2 and PD-1 blockade restrains the intratumoral accumulation of dysfunctional CD8⁺ T cells and heightens T-cell effector capacity.

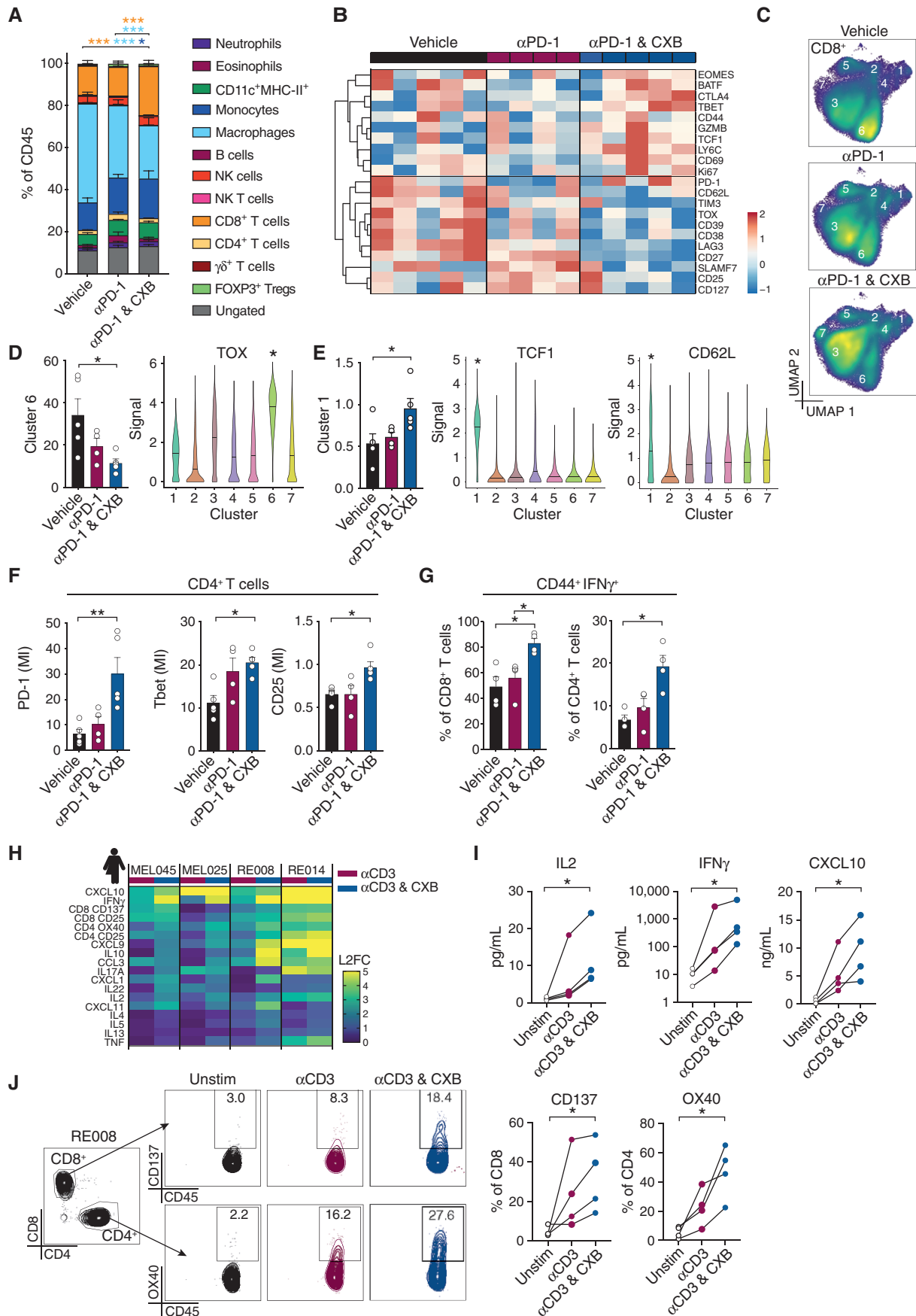
Finally, we tested whether CXB treatment could also enhance T-cell activation in the human PDTF setting. For this, we cultured PDTFs from four independent PGE₂^{hi} tumors with α CD3 in the presence or absence of CXB. Compared with α CD3 stimulation alone, the addition of CXB enhanced the production of the characteristic T-cell effector cytokines IL2 and IFN γ and the T-cell chemoattractant CXCL10 (Fig. 6H and I) and increased the expression of activation markers OX40 and CD137 on T cells (Fig. 6H and J). Together, our data support a model whereby inhibition of the COX2/PGE₂ axis rapidly and acutely shifts the tumor inflammatory landscape to promote the infiltration and activation of antitumor effector T cells, ultimately resulting in enhanced responses to immune checkpoint blockade.

DISCUSSION

Inflammation has long been described as a hallmark associated with cancer initiation, progression, recurrence, and resistance to mainstream treatments (39). Multiple studies using advanced single-cell analysis of the tumor microenvironment have elegantly characterized the phenotypic and functional diversity of tumor-infiltrating immune cells. Combined with the success of therapies targeting the host immune response, this has highlighted a dual role of inflammation in cancer (6). In recent work, we have identified COX2 activity and its associated inflammatory response as key determinants of immune escape in preclinical models and of outcomes from ICB in multiple cancer types (5, 8). Given this evidence and the widespread use of nonsteroidal and steroidal anti-inflammatory drugs that target the COX2 pathway for managing inflammation and associated pain, we investigated their effect on the intratumoral immune landscape and potential for enhancing the response to immunotherapy. Using therapeutically relevant regimens and doses, we demonstrated that targeting the COX2/PGE₂/EP2-4 axis with different types of drugs acutely shifts the tumor microenvironment and enhances the efficacy of immune checkpoint blockade.

The synergistic effect of COX2/PGE₂/EP2-4 pathway inhibition and ICB treatment was observed irrespective of the different pharmacokinetics and pharmacodynamics of the

Figure 6. COX2/PGE₂ signaling inhibition in combination with α PD-1 treatment causes a phenotypic shift in tumor-infiltrating CD8⁺ T cells. **A**, Frequency of tumor-infiltrating immune cells out of CD45⁺ cells in melanoma tumors on day 7 after treatment, as measured by CyTOF ($n = 5$ per treatment group). P value by 2-way ANOVA. **B**, Hierarchical clustering and heat map representing the mean intensity expression of select surface and intracellular markers associated with intratumoral CD8⁺ T functional states measured by CyTOF. **C**, UMAP plots displaying the relative abundance of different CD8⁺ T-cell clusters across treatment groups as defined by FLOW-SOM. **D**, Treatment-based comparison of the relative abundance of Cluster 6 within CD8⁺ T cells, which is characterized by high expression of TOX. **E**, Treatment-based comparison of the relative abundance of Cluster 1 within CD45⁺ T cells, which is characterized by high expression of CD62L and the stem-like marker TCF1. **F**, Bar plots of the median intensity (MI) of PD-1, CD25, and T-bet expression in non-Treg CD4⁺ T cells. **G**, Bar plots of the frequency of CD44⁺ IFN γ ⁺ cells within CD8⁺ or CD4⁺ T cells. **H** and **I**, Heat map representing log₂ fold-change in expression of cytokines, chemokines, and T-cell surface markers (**H**), and paired dot plots representing levels of IL2, IFN γ , and CXCL10 48 hours after anti-CD3 and/or CXB treatment of PDTFs from 4 independent tumors (**I**; averaged from 1–2 repeat cultures). **J**, Representative FACS plots and paired dot plots of OX40 (percentage of CD4) or CD137 (percentage of CD8) expression 48 hours after anti-CD3 and/or CXB treatment of PDTFs from 4 independent tumors (averaged from 1–2 repeat cultures). P value by 1-way ANOVA (**D**, **E**, **F**, **G**, **I**, **J**). Data representative of 2 independent experiments with $n = 5$ mice per group (**A–G**) or 2 independent PDTF cultures (**H–J**). *, $P < 0.05$; **, $P < 0.01$; ***, $P < 0.001$.



Downloaded from <http://aacrjournals.org/cancerdiscovery/article-pdf/11/10/2602/308227/2602.pdf> by guest on 07 November 2024

anti-inflammatory drugs tested. Most surprisingly, corticosteroids, widely considered to be potent immunosuppressants and routinely prescribed to cancer patients for the management of ICB-induced irAEs, also augmented tumor clearance after ICB with either α PD-1 or the combination of α PD-1 plus α CTLA4. This suggests that corticosteroids, while effectively limiting irAEs, might simultaneously improve the antitumor response. In line with this hypothesis, TNF blockade was recently shown to synergize with α PD-1 therapy while concomitantly dampening experimental colitis (40). Our proof-of-concept work supports preclinical evidence that corticosteroids may preserve antitumor immunity (30, 41, 42) and indicates that the use of broad anti-inflammatory drugs could paradoxically boost immune control. Although it remains to be determined in which settings this combination may work best, we speculate that corticosteroids may be beneficial where protumorigenic inflammatory responses are prevalent. Furthermore, substantial evidence exists that despite ICB treatment withdrawal, overall survival rates are comparable in immunotherapy patients receiving corticosteroids for preexisting autoimmune conditions (43, 44) or for the treatment of irAEs (16–19). Future studies in both preclinical and clinical settings will be required to reconcile all the conflicting observations and define the potential conditions in which the use of corticosteroids in patients undergoing ICB might be beneficial or should be contraindicated.

Patient and tumor characteristics such as overall burden, location, oncogenic signaling, presence of tumor-infiltrating T cells, tumor mutational burden, neoantigen clonality, and patient microbiome composition have all been shown to associate with ICB outcome (2, 45). Because of this, one of the biggest challenges in the treatment of patients with ICB is the heterogeneous response between patients (1, 28). Remarkably, even though our experiments were performed with inbred animals obtained from a single commercial vendor, housed in highly controlled conditions and bearing tumors formed by genetically identical cancer cells, we observed consistent dichotomy in ICB response across models and treatment regimens. This variability in tumor fate after treatment constitutes a major limitation to the identification of mechanisms underlying efficacy, especially at early time points after treatment when responder and nonresponder tumors are macroscopically indistinguishable. To overcome this limitation, we used a bilateral surgery model in which contralateral tumors showed highly concordant responses after ICB, in line with recent reports (31, 32). This experimental approach allowed us to classify tumors as responders or nonresponders based on the fate of the contralateral tumor.

Unbiased hierarchical *k*-means clustering of the transcriptome of surgically resected tumors early in treatment identified 2 major clusters differentially enriched in responding and nonresponding mice. The defining feature of the response cluster was the upregulation of an IFN γ -associated transcriptional program. Accordingly, tumor control after combination treatment with CXB and PD-1 blockade was impaired in mice deficient in IFN γ or lacking NK, cDC1, or adaptive immunity. These data further expose the importance of an NK/cDC1/T-cell axis in ICB-induced tumor immunity (46) and provide additional evidence for IFN γ as a primary cytokine instructing a rapid response to immune checkpoint

inhibitors (11, 12, 36). Furthermore, we found that cancer patients benefiting from ICB showed a similar enrichment in the IFN γ -driven transcriptional response program in samples both before and during treatment.

Remarkably, we showed that this response program could also be rapidly induced by inhibiting PGE₂ production or signaling in as few as 4 hours. Of note, these changes were transient and waned over time without repeated dosing, revealing a marked plasticity in the tumor immune microenvironment and indicating the need for sustained therapeutic COX2 inhibition, and potentially for twice and three-time daily dosing, to maximize its potentiating effects on ICB. These findings have direct implications for the design of treatment protocols to combine ICB and inhibitors of the COX2/PGE₂/EP2-4 axis, which are currently being tested in multiple clinical trials across cancer types (e.g., NCT03155061, NCT03026140).

The relevance of our findings for human malignancies was further demonstrated by showing that addition of CXB altered the inflammatory profile of patient tumors *ex vivo* using a recently developed PDTF platform (37). Addition of CXB reduced the production of protumorigenic mediators such as IL6 or CXCL1 while concomitantly enhancing the release of CXCL9 and CXCL10, major IFN γ -driven CD8⁺ T cell chemoattractants essential for natural and therapy-induced antitumor immunity (47). In addition, when combined with anti-CD3 stimulation, CXB further potentiated the activation of T cells present within human tumor specimens and the production of critical effector cytokines such as IFN γ or IL2.

Data from both murine and human tumors highlight the dual role of COX2 inhibitors in modulating the flavor of inflammation. We have recently shown that monitoring the ratio of these 2 opposing profiles using COX-IS constitutes a powerful strategy to predict patient survival and ICB outcome in multiple cancer types (5). Here we found that monotherapy with CXB or EPAT could rapidly lower the COX-IS, ultimately enhancing the efficacy of PD-1 blockade when used in combination. Our efforts to investigate the underpinning mechanistic basis for the synergy between ICB and anti-inflammatory drugs show that although the tumor microenvironment transcriptional profile changed rapidly following treatment, the overall leukocyte infiltrate composition was less affected. Nonetheless, multiparametric immunophenotyping by CyTOF showed that the early molecular remodeling favors the recruitment and expansion of TCF1⁺ naive-like, cytokine-producing CD8⁺ T cells, while limiting their dysfunctional phenotype.

In conclusion, across multiple models, we have identified a major role for the COX2/PGE₂/EP2-4 axis as an independent immune checkpoint that can be therapeutically targeted with widely available drugs. Of major clinical relevance, our work in both mouse and human cancer settings demonstrated that COX2 inhibition can rapidly remodel the intratumoral immune molecular profile and fuel T-cell effector function rather than indiscriminately limiting inflammation. Overall, our findings are consistent with a model whereby anti-inflammatory drugs enhance immune control by limiting COX2-driven immune evasion and tilt the balance toward cancer-inhibitory inflammation. Pharmacologic inhibition of the COX2/PGE₂ axis using readily available anti-inflammatory drugs therefore has great potential to modulate the tumor immune environment and improve the efficacy of existing immune-targeting drugs.

METHODS

Cell Lines and Cell Culture

CT26 and 4T1 cells (Cancer Research UK Manchester Institute) are commercially available. The *Braf*^{V600E}-driven 5555 melanoma cell line was established from C57BL/6 *Braf*^{V600E};*Tyr::CreERT2*^{+/+}; *p16*^{INK4a}^{-/-} mice (48). COX2^{KO} cells (CT26 and 4T1) were generated by CRISPR/Cas9-mediated genome engineering as previously described (5). To restore COX2 expression in COX2^{KO} 4T1 breast cells, the full-length (1.8-kb) open reading frame of mouse *Ptgs2* was cloned from the parental 5555 melanoma cell line and subcloned into the retroviral expression vector pFB-neo (Agilent). After retroviral transduction (see Supplementary Methods for more details), COX2^{REST} cells were selected in the presence of 300 µg/mL G-418 (Sigma). Knockout and restoration of COX2 expression were verified by immunoblotting using anti-COX2 specific antibodies (Cell Signaling, 12282) and by measuring PGE₂ in cell supernatants by ELISA (R&D Systems or Cayman Chemical; Supplementary Fig. S1A and B). Cells were maintained at low passage and cultured in standard conditions in RPMI-1640 (Lonza) supplemented with 5% penicillin/streptomycin (Thermo Fisher Scientific) and 10% fetal bovine serum (Life Technologies) and routinely confirmed to be *Mycoplasma*-free (Venor GeM gEP Mycoplasma Detection Kit, Minerva Biolabs) and mouse hepatitis virus-free (QIAamp Viral RNA Mini extraction kit, Qiagen) by qPCR. For inoculation into mice, cells were freshly thawed, grown to 80%–90% confluency before passaging, passaged ≥3 times, harvested in the exponential phase of growth by trypsinization (Sigma), washed 3 times with cold PBS (Thermo Fisher), filtered through a 70-µm filter (Thermo Fisher), and resuspended in cold PBS. For in vitro treatment of cells, lyophilized celecoxib (LC labs) and methylprednisolone (Sigma) were reconstituted in sterile DMSO. 1 × 10⁵ CT26 colorectal tumor cells were plated in a 24-well plate, left overnight, and treated with a final concentration of 5 µmol/L of CXB or 0.5 mg/mL of methylprednisolone. Both drugs were refreshed after 24 hours, and supernatants were harvested the next day and tested for PGE₂ levels.

Animal Experiments

For *in vivo* studies, female and male wild-type (C57BL/6 and BALB/c, Envigo, stock 057 and 162) and genetically modified strains (*Irfng*^{-/-}, *Rag1*^{-/-}, *Batf3*^{-/-} on C57BL/6 background and NSG bred at CRUK Manchester Institute) were assigned to experimental groups and housed under specific pathogen-free conditions and in individually ventilated cages in the institutional Biological Research Unit. 1 × 10⁵ to 5 × 10⁵ cells were injected subcutaneously in 100 µL of PBS into the right flank or bilaterally into both flanks in the surgery model (see also Supplementary Methods). No statistical analysis was performed to determine sample size. Most experiments were performed using female mice 6–10 weeks of age. Tumor size was quantified as the mean of the longest diameter (length) and its perpendicular (width) measured by a hand caliper. Stratified randomization was applied to normalize tumor sizes and body weights across treatment groups. The investigators were not blinded to allocation during experiments or outcome assessments. All procedures involving animals were performed under the PDCC31AAF license, in accordance with National Home Office regulations under the Animals (Scientific Procedures) Act 1986. Procedures were approved by the Animal Welfare and Ethical Review Body (AWERB) of the CRUK Manchester Institute, and tumor volumes did not exceed the guidelines set by the Committee of the National Cancer Research Institute (49) as stipulated by the AWERB.

In Vivo Treatments

Lyophilized celecoxib (CXB, LC Labs), EP2 antagonist (TG4-155, Cayman), and EP4 antagonist (ONO-AE3-208, ONO Pharmaceuticals) were weighed using a fine balance and made up in a 60:40

ratio of DMSO (1 part, Sigma)/PEG400 (5 parts, Sigma):dH₂O at a concentration of 3 mg/mL (200 µL/dose, 30 mpk), and administered by oral gavage once or twice daily depending on the experiment (see figure legends for details). The dose and regimen for the administration of EPAT to tumor-bearing mice were chosen based on dose-escalating pharmacokinetic studies monitoring the concentration of EP2 and EP4 antagonists in plasma. Lyophilized methylprednisolone (Solu-Medrone, Pfizer UK) was weighed and made up in PBS at a concentration of 1 mg/5 mL (1 mpk, 20 µg/dose) or 100 mg/5 mL (100 mpk, 200 µg/dose) and injected intraperitoneally (i.p.) in 100 µL for 2–5 days depending on the experiment. After 5 days of treatment with methylprednisolone, prednisolone oral solution (Logixx Pharma Solutions) was diluted in PBS to a concentration of 0.1 mg/mL, and mice were dosed with 200 µL per os (1 mpk, 20 µg/dose) for ≤16 days. Mice were injected with 200 µg of αPD-1 (RMP1-14, BioXcell) alone or in combination with 100 µg αCTLA4 (9D9, BioXcell) twice weekly for ≤6 doses. An alternative αPD-1 clone (4H2, Ono Pharmaceutical) was also tested alone or in combination with EPAT, achieving similar results as the BioXcell clone. For NK cell depletion, mice were injected i.p. with a single dose of 200 µg of anti-NK1.1 (PK136, BioXcell, BE0036) and 50 µL anti-ASIALO-GM-1 (BioLegend, 146002) either 1 day before treatment, for transcriptomic analysis, or 1 day before inoculation of cells, followed by biweekly treatment for tumor growth studies.

RNA Isolation and qPCR

Tumors were collected in PureZOL Reagent (Bio-Rad) and stored at –80°C. For processing, tumors were dissociated with 5-mm stainless steel beads (Qiagen) using the TissueLyser II (Qiagen). Total RNA was extracted using the Direct-zol RNA Mini Prep Kit (Zymo Research) following the manufacturer's recommendations, including a DNase digestion step. RNA was quantified using a NanoDrop One (Thermo Fisher) or a Bioanalyzer (Agilent Technologies) for RNA-seq. For qPCR, cDNA was synthesized using 1–2 µg × of total RNA by reverse transcription using High Capacity cDNA archive kit (Applied Biosystems), including an RNase inhibitor (Promega). Quantitative real-time PCR was performed using TaqMan probes (Applied Biosystems) and either TaqMan Universal PCR MasterMix when run on the QS5 fast real-time PCR system (Applied Biosystems) or consumables from the 96.96 Dynamic array when run on the Biomark HD system (Fluidigm). Data were analyzed with the Δ2CT method (Applied Biosystems, Real-Time PCR Applications Guide). Z-score normalization was performed to pool experiments, and cumulative z scores were calculated by adding z scores of multiple markers per individual mouse. The COX-IS ratio was calculated as previously described (5).

RNA-seq and Analysis in Mouse Tumors

For bulk RNA-seq, mRNA libraries were prepared using Lexogen QuantSeq 3'-mRNAseq Library Prep Kit (Illumina) from 500 ng total RNA, quantified by Bioanalyzer, and sequenced on the Illumina NextSeq500. RNA-seq reads were quality checked using FastQC version 2.17.1.14 (<https://www.bioinformatics.babraham.ac.uk/projects/fastqc/>), trimmed using Trim Galore version 0.6.5, and aligned in single-end mode to the mouse genome assembly (GRCm38.75) using the STAR aligner version 2.6.1d with default parameters. Mapped data were converted to gene level integer read counts (expression) using featureCounts and Ensemble GTF annotation (Mus_musculus.GRCm38.75.gtf). featureCounts were preprocessed (minimum CPM of 0.5 in ≥3 samples) and normalized using the voom model in the limma package of Bioconductor. Unsupervised clustering analysis by nonnegative matrix factorization (NMF consensus; <https://www.genepattern.org>) method was performed to identify the presence of potential transcriptional programs associated with outcome/treatment. Enrichment of molecular pathways

(MSigDB) was evaluated by GSEA using the GenePattern Analytical Toolkit (<https://www.genepattern.org>). Differential gene expression analysis was performed using comparative marker selection method (Gene Pattern modules, <https://www.genepattern.org>) and DESeq2 package from Bioconductor. DEGs were defined based on linear fold change ± 1.5 , and P value/false discovery rate < 0.05 . The resulting gene list was analyzed with IPA software. Estimation of cell types in the tumor microenvironment was performed using the MCP-counter (33) and Consensus (34) methods to determine the relative abundance of 10 cell types and a general immune score of the total level of immune cell infiltration in each tumor sample, respectively.

Transcriptomic Analysis in Human Patient Datasets

Details of publicly available RNA-seq datasets of cancer patients receiving ICB can be found in Supplementary Table S4. When applicable, RNA-seq reads were processed and mapped as described above using the human genome assembly (Homo sapiens.GRCh38) for mapping and annotation. Processing and normalization of raw feature count matrices were performed using the edgeR package (version 3.24.3). Genes were filtered out based on a threshold of 0.25 CPM in 10% samples. A \log_2 CPM+1 expression matrix was generated and used for downstream analysis. Alternatively, if available, normalized FPKM and TPM values were obtained from the Gene Expression Omnibus database. For AIR enrichment analysis by GSEA, partial or complete responses were pooled as responders, and progressive disease and stable disease as nonresponders.

FACS Analysis

For analysis of tumor-infiltrating leukocytes, tumors were collected into ice-cold RPMI-1640 on ice. The surface of the tumor samples was dried with paper, and the tumor weight was recorded. Samples were transferred into C-tubes (Miltenyi Biotech) containing RPMI-1640, Collagenase IV (200 U/mL, Worthington Biochemical), and DNase I (0.2 mg/mL, Roche) and minced using scissors. The C-tubes were placed in a GentleMACS Octo Dissociator (Miltenyi Biotech), and tumors disaggregated with 2 rounds of the automated program *m_impTumor_02_01*. Dissociated tumors were incubated for 35 minutes at 37°C and disaggregated for one more round. The C-tubes were centrifuged, and pellets were resuspended in cold RPMI-1640 before being filtered through a 70- μ m cell strainer and pelleted. Cell suspensions were resuspended in PBS for CyTOF or FACS buffer (PBS containing 2% FCS, 2 mmol/L EDTA, and 0.01% sodium azide) for flow cytometry analysis. Fc receptors were blocked with anti-CD16/32 (2.4G2, eBioscience) 5 minutes before staining. Cell viability was determined by Aqua LIVE/Dead-405 nm staining (Invitrogen). Tumors were stained with combinations of the following antibodies: CD45-BV605 (30-F11), CD11b-BV785 (M1/70), Ly6G-PE-CF594 (1A8), Ly6C-FITC (AL-21), F4/80-PE-Cy7 (CI: A3-1) anti-MHCII I-A/I-E APC-eFluor780 (114.15.2), anti-CD11c-PerCP/Cy5.5 (N418), anti-CD103 PE (2E7), NK1.1-APC (PK136), CD49b-APC (DX5), XCR1-BV421 (ZET), CD3e PercCP-Cy5.5 (145-2C11), CD8 α -PE (53-6.7), CD4-FITC (RM4-5), CD44-APC-eFluor780 (IM7), and IFN γ -eFluor450 (XMG1.2) from eBioscience or BioLegend. For intracellular cytokine detection, cells were stimulated *ex vivo* for 4 hours with Cell Stimulation Cocktail (Thermo Fisher) and stained using the Intracellular Fixation & Permeabilization Buffer Set (eBioscience) following manufacturer instructions. Monensin (BioLegend) and Brefeldin A (BioLegend) solutions were added 2 hours before staining, and nonspecific binding of intracellular epitopes was blocked by preincubation of cells with 2% normal rat serum (Thermo Fisher). Live cell counts were calculated from the acquisition of a fixed number (5,000) of 10- μ m latex beads (Beckman Coulter) mixed with a known volume of cell suspension. Spectral overlap was calculated using live cells or VersaComp antibody capture beads (Beckman Coulter). Cells were acquired on a Fortessa X-20 (BD Bioscience) or

a Novocyte (ACEA). Flow cytometry standard .fcs files were analyzed using FlowJo version 10.6.2 (TreeStar).

Multiplexed Immunofluorescence

Multiplexed Tyramide Signal Amplification (TSA) immunofluorescence staining was performed using the BOND RX automated platform (Leica Microsystems). Four-micron-thick sections of formalin-fixed, paraffin-embedded tumors were cut and mounted on charged slides. Dewaxing and heat-induced epitope retrieval (HIER) of slides was automated on the Bond RX using epitope solution 1 (AR9961) for 20 minutes at 100°C. Using the Open Research Kit (DS9777), endogenous peroxidase was blocked using 3% hydrogen peroxide (VWR) for 10 minutes, and the slides were further blocked with 10% (w/v) casein (Vector SP5020 in TBST). Antibody application and detection and TSA amplification were conducted in sequential rounds following the same general procedure: incubation with the primary antibody in Bond antibody diluent (AR9352) for 30 minutes (in the following sequence: CD8 5 μ g/mL [eBioscience, 14-0808], CD4 5 μ g/mL [eBioscience, 14-9766], and FOXP3 2.5 μ g/mL [eBioscience, 14-5773-82], followed by detection using anti-rat ImmPRESS HRP (Vector MP5444; RTU) for 30 minutes, followed by premixed TSA reagent (PerkinElmer) 1/200 for 10 minutes. Antibody sequence and TSA-fluorophore selection were optimized to reduce nonspecific staining and tyramide binding site competition. After labeling with TSA, each antibody was removed using a heat stripping step (epitope solution 1 [AR9961] for 10 minutes at 100°C). Finally, nuclei were counterstained with DAPI (Thermo Fisher, 62248) for 15 minutes (0.33 μ g/mL) and mounted on coverslips with ProLong Gold antifade mountant (Thermo Fisher, P36930). Images were scanned at 20 \times on an Aperio VERSA (Leica Biosystems), then analyzed and quantified using the HALO® (Indica Labs) Highlex FL module.

Analysis of PDTFs

Patient Characteristics and Tumor Sample Processing. Tumor samples were collected from individuals with melanoma, non-small cell lung cancer, ovarian cancer, and colorectal or renal cell carcinoma undergoing surgical treatment between September 2017 and August 2020 at the Netherlands Cancer Institute (NKI-AVL), Netherlands. The study was approved by the NKI-AVL review board and performed in compliance with all relevant ethical regulations. Patient characteristics are provided in Supplementary Table S5. All studies were performed in compliance with ethical regulations, and patients consented to the research usage of material not required for diagnostics either by opt-out procedure or upon prior written informed consent (after May 23, 2018). Tumor sample processing and storage were done as described (37). Briefly, solid tumor lesions were identified by a pathologist. One part of the tumor was embedded in paraffin for histologic analysis, and the other part was processed by manual cutting into small tumor fragments of 1–2-mm³ size on ice. Subsequently, PDTFs from different areas were mixed and frozen in cryovials containing 1 mL of freezing medium (FBS with 10% DMSO, Sigma), with 8–15 PDTFs per vial. The vials were cryopreserved in liquid nitrogen until further use.

Ex Vivo Cultures. PDTF cultures were performed as described (37). In brief, PDTFs were slowly thawed and extensively washed in medium (DMEM, Thermo Fisher) supplemented with 1 mmol/L sodium pyruvate (Sigma), 1 \times MEM non-essential AA (Sigma), 2 mmol/L L-glutamine (Thermo Fisher), 10% FBS (Sigma), and 1% penicillin-streptomycin (Roche). Subsequently, PDTFs were embedded in an artificial extracellular matrix as follows: first, collagen I (Corning; 1 mg/mL final concentration), sodium bicarbonate (Sigma, 1.1% final concentration), and tumor medium were combined on ice, then slowly added to ice-cold Matrigel (Matrix High Concentration, Phenol Red-Free, BD Biosciences, 4 mg/mL final concentration) to

form the final matrix. After preparation of the matrix on ice, a 96-well flat-bottom plate was coated with a bottom layer of 40 μ L matrix, which was solidified by incubating for 30 minutes at 37°C. One PDTF per well was placed on top of the matrix, followed by addition of a second layer of 40 μ L matrix. After subsequent solidification at 37°C for 30 minutes, 120 μ L tumor medium was added to each well. For stimulated conditions, the medium was supplemented with anti-CD3 (OKT3, BioLegend) at a final concentration of 2 μ g/mL, CXB (LC labs) at a final concentration of 5 μ mol/L, or a combination of anti-CD3 and CXB. PDTFs were incubated for 48 hours at 37°C before readout.

Flow Cytometry Analysis. PDTFs were analyzed by flow cytometry using the following antibodies: anti-CD45 PerCP Cy5.5 (2D1), from Invitrogen; anti-CD8 BUV563 (RPA-T8), anti-PD-1 PE-Cy7 (EH12.1), anti-CD137 PE (4B4-1), all from BD Biosciences; anti-CD3 FITC (SK7), anti-CD8 BV605 (RPA-T8), anti-CD4 BV421 (SK3), anti-CD19 BV605 (SJ25C1), anti-FOXP3 AF647 (259D), anti-CD11c PE (Bu15), anti-CD16 Alexa Fluor 700 (3G8); anti-OX40 APC (BerACT35), and anti-CD25 AF700 (BC96), all from BioLegend. For analysis of immune cell composition, either PDTFs were thawed as described above or cultured PDTFs were retrieved from the matrix and pooled for each experimental condition. Next, the PDTFs were processed into single-cell suspensions by enzymatic digestion, washed, and filtered over a 150- μ m filter mesh. Cells were incubated with Fc receptor blocking agent (eBioscience) and Zombie UV (BioLegend) or Live/Dead Near-IR Dye (Thermo Fisher) for 20 minutes at 4°C. Cells were subsequently washed and resuspended in 50 μ L of staining buffer containing the above antibodies and incubated for 20 minutes at 4°C. Cells were then washed, fixed, and permeabilized using Fix/Perm solution (eBioscience) for 30 minutes at room temperature. After washing, cells were resuspended in Permeabilization Buffer (eBioscience) containing intracellular antibodies and incubated for 40 minutes at room temperature. Lastly, cells were washed before data acquisition. Data acquisition was performed using a BD LSR II SORP or a Fortessa SORP cell analyzer (BD Biosciences). Data were collected using BD FACS Diva Software version 8.0.1 (LSR II SORP) and version 8.0.2 (Fortessa SORP) and analyzed with FlowJo version 10.6.1 (TreeStar).

Assessment of Soluble Mediators and PGE₂ Levels. Culture supernatant was taken after 48 hours from PDTF single wells, stored at -80°C, and thawed for assessment of cytokines, chemokines, or PGE₂ levels. Presence of indicated cytokines and chemokines was detected using the LEGENDplex Human Th Cytokine and Human Proinflammatory Chemokine panels (both from BioLegend). Levels of PGE₂ in supernatants were determined as described above.

Mass Cytometry Methods

Antibodies and Antibody Conjugation. Antibody information is listed in Supplementary Table S6. Where indicated, antibodies were purchased pre-conjugated (Fluidigm). In-house conjugations were performed using Maxpar X8 Antibody Conjugation Kits (Fluidigm), with the addition of an equal volume of PBS-based Antibody Stabilization Buffer (Candor Biosciences, 13150) containing 0.6 mg/mL sodium azide (Sigma Aldrich, S8032). To generate cisplatin conjugates, 200 μ g of antibody was reduced as in the method above, incubated with 200 μ L of 400 μ mol/L monoisotopic cisplatin (Buyl-sotope, custom order) in C-buffer from the Antibody Conjugation Kits at 37°C for 90 minutes, washed, and stored as for the polymer/lanthanide conjugates. Antibodies were titrated in panels by staining samples of known positive and negative controls.

Live/Dead and Extracellular Staining. To label cells in S-phase, mice were injected with 10 mg/mL of 5-iodo-2'-deoxyuridine (IdU; Sigma Aldrich, 17125) prepared in a minimally basic solution of 0.01 mol/L sodium hydroxide (NaOH; Sigma Aldrich, 757527) in water, 2 hours

before the mouse was culled by Schedule 1 method, and tissues were collected. Tumors were dissociated as described above. Live cells were spun at 300 \times g for 6 minutes, and fixed cells were spun at 1,000 \times g for 6 minutes. The disaggregated tumor cell pellet was resuspended in 300 μ L of ice-cold PBS and vortexed well, and 300 μ L of 1 μ mol/L 198Pt monoisotopic cisplatin (Fluidigm, 201198) in PBS was added, followed by vortexing. After 1 minute incubation, the staining was quenched with 20 mL of CSM-E (Cell Staining Buffer-Extracellular) consisting of 5 mg/mL BSA (Sigma Aldrich, A3294), 0.5% (v/v) FBS (Thermo Fisher), and 0.2 mg/mL DNase1 in PBS. The cells were counted, and 3 \times 10⁶ cells were aliquoted into a 5-mL polypropylene FACS tube, washed with 3 mL CSM-E, and pelleted. The cells were incubated in 20 μ L of 100 U/mL heparin sodium salt (Sigma Aldrich, H3393) in PBS for 5 minutes on ice, followed by metal-conjugated anti-CD64 antibody for 10 minutes on ice, followed by unconjugated anti-CD16/32 antibody for 5 minutes on ice, before adding the remaining master mix of extracellular antibodies in 50 μ L CSM-E (see Supplementary Table S6). After 45 minutes on ice, the cells were washed twice with 4 mL of CSM-E and fixed/permed using FOXP3 Fixation/Permeabilization Kit (Thermo Fisher) following manufacturer's instructions. After permeabilization, the cell pellet was resuspended in 1 mL of 10% (v/v) DMSO (Sigma Aldrich) in CSM-I (Cell Staining Buffer-Intracellular), consisting of 5 mg/mL BSA and 0.2 mg/mL sodium azide in PBS, vortexed, and frozen at -80°C.

Barcoding, Pooling, and Intracellular Staining. Cells were thawed at room temperature and washed with 4 mL PBS. The pellet for each sample was barcoded using the Cell-ID 20-plex Pd Barcoding Kit (Fluidigm, 201060) following manufacturer's instructions and washed twice with CSM-I. Samples were pooled in FOXP3 Permeabilization Buffer and pelleted. For each sample included in the pooled sample, 10 μ L of 100 U/mL heparin sodium salt in PBS and 0.5 μ L of Fc block was added, and the sample was mixed by gentle rocking. After incubating for 5 minutes at room temperature in the dark, a master mix of intracellular targeting, metal-conjugated antibodies (see Supplementary Table S6) in CSM-I was added. For each sample included in the pooled sample, 1 equivalent of antibody and 25 μ L of CSM-I was used. After 45 minutes of incubation, the cells were washed twice with 4 mL of CSM-I and fixed in 4% PFA (Thermo Fisher). The sample was vortexed and stored overnight at 4°C.

DNA Staining and Acquisition. On the day of acquisition, 0.5 μ L of 125 μ mol/L Cell-ID Iridium Intercalator (Fluidigm, 201192A) for each individual sample included in the pooled sample was added to the cell/PFA mixture and vortexed. After 1 hour of incubation at room temperature, the cells were washed once with CSM-I, aliquoted, and kept on ice until ready to run each tube. Each cell pellet was washed twice with water and resuspended at a concentration of 1 \times 10⁶ cells/mL in 15% EQ Four Element Calibration Beads (Fluidigm, 201078) in water, filtered twice through 70- μ m Filcons (BD Biosciences, 340633), and acquired on a Helios Mass Cytometer (Fluidigm), using a Super Sampler (Victorian Airship & Scientific Apparatus) at a maximum of 500 events/seconds.

Data Processing and Analysis. FCS files were normalized for signal drift during the acquisition run using the built-in Helios normalization tool (Fluidigm), and individual sample events were deconvoluted using the stand-alone debarcoder (50), with a Mahalanobis distance of 15 and a minimum barcode separation of 0.26. Individual sample FCS files were uploaded to Cytobank (<https://www.cytobank.org>, Beckman Coulter). As per standard methods, live cell events were selected based on 191Ir positivity and 198Pt negativity. 191Ir⁺ debris and cell doublets and aggregates were removed based on event length. If possible, target cells were selected by manual biaxial gating: T-cell events selected as CD45⁺CD3e⁺, further divided in CD8⁺ and CD4⁺ T cells. Target cells were exported as FCS files and uploaded to the

Cytofit2 package (version 2.0.1). Cells were clustered using unsupervised self-organizing map clustering (FLOWSOM) and visualized using UMAP projections and expression overlays, exporting cell data with annotated clusters for further downstream analysis. Plotting and statistical analysis was done using R statistical software, and the result files were exported from Cytofit2. Violin plots and expression plots were generated using the ggplot2 package in R with expression data transformed by cytofAsinh method. For cross-cluster phenotype comparison between experimental groups, the FCS files exported from Cytofit2 including the cluster annotation were loaded in Cytobank, and the cells with the phenotypes of interest were gated manually (i.e., positive cells for a specific marker or S-phase cells as IdU+ Ki-67⁺). The percentage of cells with the phenotype of interest and the median mass intensity (MMI) were calculated for each cluster. Comparisons were performed using Kruskal–Wallis test and Dunn test for pairwise comparisons with Holm-adjusted *P* values.

Statistical Analysis

Graphs were plotted using Prism version 8.4.1 (GraphPad Software) and R software (R Project). Statistics were calculated with Prism and values expressed as mean ± SEM of biological replicates. Data were analyzed with the following tests (see figure legends for details): unpaired Student *t* test, Mann–Whitney *U* test in the case of non–Gaussian-distributed data; one-way ANOVA adjusted for multiple comparisons using the Kruskal–Wallis test, and log-rank (Mantel–Cox) for the analysis of Kaplan–Meier survival curves. A *P* value <0.05 (*, *P* < 0.05; **, *P* < 0.01; ***, *P* < 0.001; ****, *P* < 0.0001) was considered significant.

Data Availability

RNA-seq data have been deposited in NCBI Gene Expression Omnibus database and can be accessed through accession number GSE160789. The accession number for bulk tumor transcriptomes of surgically excised CT26 colorectal tumors treated with αPD-1 and/or CXB is SubSeries GSE160785. The accession number for bulk tumor transcriptomes of 5555 melanoma tumors treated with vehicle, αPD-1, or EPAT is SubSeries GSE160788.

Authors' Disclosures

S. Zelenay reports a grant from Ono Pharmaceutical. E. Bonavita, C.P. Bromley, and S. Zelenay have a patent application (WO2019243567A1) on the COX-1S. Outside this current work, D.S. Thommen received research support from Bristol Myers Squibb and T.N. Schumacher receives research support from Merck KGaA; is advisor for Adaptive Biotechnologies; is advisor and stockholder in Allogene. Therapeutics, Merus, Neogene Therapeutics and Scenic Biotech; and is venture partner at Third Rock Ventures. The other authors declare no competing interests.

Authors' Contributions

V.S. Pelly: Conceptualization, formal analysis, investigation, methodology, writing–original draft, writing–review and editing. **A. Moeini:** Conceptualization, formal analysis, investigation, methodology, writing–original draft, writing–review and editing. **L.M. Roelofsen:** Formal analysis, investigation, methodology, writing–review and editing. **E. Bonavita:** Investigation, methodology, writing–review and editing. **C.R. Bell:** Investigation, methodology, writing–review and editing. **C. Hutton:** Investigation, methodology, writing–review and editing. **A. Blanco-Gomez:** Investigation, methodology, writing–review and editing. **A. Banyard:** Methodology, writing–review and editing. **C.P. Bromley:** Investigation, methodology, writing–review and editing. **E. Flanagan:** Investigation, methodology, writing–review and editing. **S. Chiang:** Investigation, methodology, writing–review and editing. **C. Jorgensen:** Supervision, funding acquisition, methodology, writing–review and editing.

T.N. Schumacher: Supervision, funding acquisition, methodology, writing–review and editing. **D.S. Thommen:** Formal analysis, supervision, funding acquisition, investigation, methodology, writing–review and editing. **S. Zelenay:** Conceptualization, supervision, funding acquisition, writing–original draft, project administration, writing–review and editing.

Acknowledgments

This work was supported by Cancer Research UK Institute Award (A19258; to V.S. Pelly, A. Moeini, E. Bonavita, C. Hutton, A. Blanco-Gomez, A. Banyard, C.R. Bell, E. Flanagan, S.-C. Chiang, C. Jørgensen, and S. Zelenay), a research agreement with Ono Pharmaceutical (to A. Moeini and S. Zelenay), an ERC CoG Disect (772577; to C. Jørgensen), a KWF Young investigator grant 12046 (to D.S. Thommen), and ERC AdG SENSIT (to T.N. Schumacher). V.S. Pelly received additional support from a CRUK Travel award (C69793/A28996), E. Bonavita from an EMBO long-term fellowship (ALTF-69-2016) and an EMBO advanced fellowship (aALTF-638-2018), and C.P. Bromley from the NIHR Manchester Biomedical Research Centre. We thank colleagues in the CRUK Manchester Institute Core facilities (Biological Resource Unit, Transgenic Breeding, Molecular Biology, Histology, Flow Cytometry and Visualisation, Irradiation and Analysis) for their support.

The costs of publication of this article were defrayed in part by the payment of page charges. This article must therefore be hereby marked *advertisement* in accordance with 18 U.S.C. Section 1734 solely to indicate this fact.

Received December 18, 2020; revised March 24, 2021; accepted May 14, 2021; published first May 24, 2021.

REFERENCES

- Ribas A, Wolchok JD. Cancer immunotherapy using checkpoint blockade. *Science* 2018;359:1350–5.
- Kalbasi A, Ribas A. Tumour-intrinsic resistance to immune checkpoint blockade. *Nat Rev Immunol* 2020;20:25–39.
- Postow MA, Sidlow R, Hellmann MD. Immune-related adverse events associated with immune checkpoint blockade. *N Engl J Med* 2018;378:158–68.
- Galon J, Bruni D. Approaches to treat immune hot, altered and cold tumours with combination immunotherapies. *Nat Rev Drug Discov* 2019;18:197–218.
- Bonavita E, Bromley CP, Jonsson G, Pelly VS, Sahoo S, Walwyn-Brown K, et al. Antagonistic inflammatory phenotypes dictate tumor fate and response to immune checkpoint blockade. *Immunity* 2020;53:1215–29.
- Shalpour S, Karin M. Pas de Deux: control of anti-tumor immunity by cancer-associated inflammation. *Immunity* 2019;51:15–26.
- Wang D, DuBois RN. Role of prostanoids in gastrointestinal cancer. *J Clin Invest* 2018;128:2732–42.
- Zelenay S, van der Veen AG, Böttcher JP, Snelgrove KJ, Rogers N, Acton SE, et al. Cyclooxygenase-dependent tumor growth through evasion of immunity. *Cell* 2015;162:1257–70.
- Zelenay S, Reis e Sousa C. Reducing prostaglandin E2 production to raise cancer immunogenicity. *Oncoimmunology* 2016;5:e1123370.
- Böttcher JP, Bonavita E, Chakravarty P, Blees H, Cabeza-Cabrero M, Sammicheli S, et al. NK cells stimulate recruitment of cDC1 into the tumor microenvironment promoting cancer immune control. *Cell* 2018;172:1022–37.
- Ayers M, Luceford J, Nebozhyn M, Murphy E, Loboda A, Kaufman DR, et al. IFN-γ-related mRNA profile predicts clinical response to PD-1 blockade. *J Clin Invest* 2017;127:2930–40.
- Grasso CS, Tsoi J, Onyshchenko M, Abril-Rodriguez G, Ross-Macdonald P, Wind-Rotolo M, et al. Conserved interferon-γ signaling drives clinical response to immune checkpoint blockade therapy in melanoma. *Cancer Cell* 2020;38:500–15.

13. Rhen T, Cidlowski JA. Antiinflammatory action of glucocorticoids – new mechanisms for old drugs. *N Engl J Med* 2005;353:1711–23.
14. Wang DY, McQuade JL, Rai RR, Park JJ, Zhao S, Ye F, et al. The impact of nonsteroidal anti-inflammatory drugs, beta blockers, and metformin on the efficacy of anti-PD-1 therapy in advanced melanoma. *Oncologist* 2020;25:e602–5.
15. Wang SJ, Khullar K, Kim S, Yegya-Raman N, Malhotra J, Groisberg R, et al. Effect of cyclo-oxygenase inhibitor use during checkpoint blockade immunotherapy in patients with metastatic melanoma and non-small cell lung cancer. *J Immunother Cancer* 2020;8:e000889.
16. Schadendorf D, Wolchok JD, Stephen Hodi F, Chiarion-Sileni V, Gonzalez R, Rutkowski P, et al. Efficacy and safety outcomes in patients with advanced melanoma who discontinued treatment with nivolumab and ipilimumab because of adverse events: a pooled analysis of randomized phase II and III trials. *J Clin Oncol* 2017;35:3807–14.
17. Sznol M, Ferrucci PF, Hogg D, Atkins MB, Wolter P, Guidoboni M, et al. Pooled analysis safety profile of nivolumab and ipilimumab combination therapy in patients with advanced melanoma. *J Clin Oncol* 2017;35:3815–22.
18. Horvat TZ, Adel NG, Dang TO, Momtaz P, Postow MA, Callahan MK, et al. Immune-related adverse events, need for systemic immunosuppression, and effects on survival and time to treatment failure in patients with melanoma treated with ipilimumab at memorial sloan kettering cancer center. *J Clin Oncol* 2015;33:3193–8.
19. Weber JS, Hodi FS, Wolchok JD, Topalian SL, Schadendorf D, Larkin J, et al. Safety profile of nivolumab monotherapy: a pooled analysis of patients with advanced melanoma. *J Clin Oncol* 2017;35:785–92.
20. Markosyan N, Li J, Sun YH, Richman LP, Lin JH, Yan F, et al. Tumor cell-intrinsic EPHA2 suppresses antitumor immunity by regulating PTGS2 (COX-2). *J Clin Invest* 2019;129:3594–609.
21. Kim S-H, Roszik J, Cho S-N, Ogata D, Milton DR, Peng W, et al. The COX2 effector microsomal PGE2 synthase 1 is a regulator of immunosuppression in cutaneous melanoma. *Clin Cancer Res* 2019;25:1650–63.
22. Li Y, Fang M, Zhang J, Wang J, Song Y, Shi J, et al. Hydrogel dual delivered celecoxib and anti-PD-1 synergistically improve antitumor immunity. *Oncoimmunology* 2015;5:e1074374.
23. Hou W, Sampath P, Rojas JJ, Thorne SH. Oncolytic virus-mediated targeting of PGE2 in the tumor alters the immune status and sensitizes established and resistant tumors to immunotherapy. *Cancer Cell* 2016;30:108–19.
24. Nissen SE, Yeomans ND, Solomon DH, Lüscher TF, Libby P, Husni ME, et al. Cardiovascular safety of celecoxib, naproxen, or ibuprofen for arthritis. *N Engl J Med* 2016;375:2519–29.
25. Brahmer JR, Lacchetti C, Schneider BJ, Atkins MB, Brassil KJ, Caterino JM, et al. Management of immune-related adverse events in patients treated with immune checkpoint inhibitor therapy: American society of clinical oncology clinical practice guideline. *J Clin Oncol* 2018;36:1714–68.
26. Frijters R, Fleuren W, Toonen EJM, Tuckermann JP, Reichardt HM, van der Maaden H, et al. Prednisolone-induced differential gene expression in mouse liver carrying wild type or a dimerization-defective glucocorticoid receptor. *BMC Genomics* 2010;11:359.
27. Cain DW, Cidlowski JA. Immune regulation by glucocorticoids. *Nat Rev Immunol* 2017;17:233–47.
28. Larkin J, Chiarion-Sileni V, Gonzalez R, Grob J-J, Rutkowski P, Lao CD, et al. Five-year survival with combined nivolumab and ipilimumab in advanced melanoma. *N Engl J Med* 2019;381:1535–46.
29. Bauché D, Mauze S, Kochel C, Grein J, Sawant A, Zybina Y, et al. Antitumor efficacy of combined CTLA4/PD-1 blockade without intestinal inflammation is achieved by elimination of Fc 3R interactions. *J Immunother Cancer* 2020;8:e001584.
30. Tokunaga A, Sugiyama D, Maeda Y, Warner AB, Panageas KS, Ito S, et al. Selective inhibition of low-affinity memory CD8+ T cells by corticosteroids. *J Exp Med* 2019;216:2701–13.
31. Zemek RM, Fear VS, Forbes C, de JE, Casey TH, Boon L, et al. Bilateral murine tumor models for characterizing the response to immune checkpoint blockade. *Nat Protoc* 2020;15:1628–48.
32. Zemek RM, De JE, Chin WL, Schuster IS, Fear VS, Casey TH, et al. Sensitization to immune checkpoint blockade through activation of a STAT1/NK axis in the tumor microenvironment. *Sci Transl Med* 2019;11:eaav7816.
33. Becht E, Giraldo NA, Lacroix L, Buttard B, Elarouci N, Petitprez F, et al. Estimating the population abundance of tissue-infiltrating immune and stromal cell populations using gene expression. *Genome Biol* 2016;17:218.
34. Jimenez-Sanchez A, Cast O, Miller ML. Comprehensive benchmarking and integration of tumor microenvironment cell estimation methods. *Cancer Res* 2019;79:6238–46.
35. Cannon CP, Cannon PJ. Physiology: COX-2 inhibitors and cardiovascular risk. *Science* 2012;336:1386–7.
36. Garris CS, Arlauckas SP, Kohler RH, Trefny MP, Garren S, Piot C, et al. Successful anti-PD-1 cancer immunotherapy requires T cell-dendritic cell crosstalk involving the cytokines IFN- γ and IL-12. *Immunity* 2018;49:1148–61.
37. Voabil P, de Bruijn M, Roelofsen LM, Hendriks SH, Brokamp S, van den Braber M, et al. An ex vivo tumor fragment platform to dissect response to PD-1 blockade in cancer. *Nat Med* 2021;27:1250–61.
38. van der Leun AM, Thommen DS, Schumacher TN. CD8+ T cell states in human cancer: insights from single-cell analysis. *Nat Rev Cancer* 2020;20:218–32.
39. Hanahan D, Weinberg RA. Hallmarks of cancer: the next generation. *Cell* 2011;144:646–74.
40. Perez-Ruiz E, Minute L, Otano I, Alvarez M, Ochoa MC, Belsue V, et al. Prophylactic TNF blockade uncouples efficacy and toxicity in dual CTLA-4 and PD-1 immunotherapy. *Nature* 2019;569:428–32.
41. Hinrichs CS, Palmer DC, Rosenberg SA, Restifo NP. Glucocorticoids do not inhibit antitumor activity of activated CD8+ T cells. *J Immunother* 2005;28:517–24.
42. Maxwell R, Luksik AS, Garzon-Muvdi T, Hung AL, Kim ES, Wu A, et al. Contrasting impact of corticosteroids on anti-PD-1 immunotherapy efficacy for tumor histologies located within or outside the central nervous system. *Oncoimmunology* 2018;7:e1500108.
43. Johnson DB, Sullivan RJ, Ott PA, Carlino MS, Khushalani NI, Ye F, et al. Ipilimumab therapy in patients with advanced melanoma and preexisting autoimmune disorders. *JAMA Oncol* 2016;2:234–40.
44. Menzies AM, Johnson DB, Ramanujam S, Atkinson VG, Wong ANM, Park JJ, et al. Anti-PD-1 therapy in patients with advanced melanoma and preexisting autoimmune disorders or major toxicity with ipilimumab. *Ann Oncol* 2017;28:368–76.
45. Havel JJ, Chowell D, Chan TA. The evolving landscape of biomarkers for checkpoint inhibitor immunotherapy. *Nat Rev Cancer* 2019;19:133–50.
46. Barry KC, Hsu J, Broz ML, Cueto FJ, Binnewies M, Combes AJ, et al. A natural killer–dendritic cell axis defines checkpoint therapy–responsive tumor microenvironments. *Nat Med* 2018;24:1178–91.
47. Chow MT, Ozga AJ, Servis RL, Frederick DT, Lo JA, Fisher DE, et al. Intratumoral activity of the CXCR3 chemokine system is required for the efficacy of anti-PD-1 therapy. *Immunity* 2019;50:1498–512.
48. Dhomen N, Reis-Filho JS, da Rocha Dias S, Hayward R, Savage K, Delmas V, et al. Oncogenic Braf induces melanocyte senescence and melanoma in mice. *Cancer Cell* 2009;15:294–303.
49. Workman P, Aboagye EO, Balkwill F, Balmain A, Bruder G, Chaplin DJ, et al. Guidelines for the welfare and use of animals in cancer research. *Br J Cancer* 2010;102:1555–77.
50. Zunder ER, Finck R, Behbehani GK, Amir EAD, Krishnaswamy S, Gonzalez VD, et al. Palladium-based mass tag cell barcoding with a doublet-filtering scheme and single-cell deconvolution algorithm. *Nat Protoc* 2015;10:316–33.